

The Effect of Hyperdiffusion on Rotating Rayleigh-Bénard Convection*

B. Davy[†]

*EPSRC Centre for Doctoral Training in Fluid Dynamics,
University of Leeds, Leeds LS2 9JT, UK*

C. J. Davies and J. E. Mound

School of Earth and Environment, University of Leeds, Leeds LS2 9JT, UK

S. M. Tobias

*Department of Applied Mathematics,
University of Leeds, Leeds LS2 9JT, UK*

(Dated: December 11, 2025)

Abstract

We analyse the effect of a scale-dependent horizontal hyperdiffusivity in rotating Rayleigh-Bénard convection. The hyperdiffusion (HD) is parameterised by a cutoff wavenumber k_0 and a growth rate q to limit its effects to the smaller scales, enabling simulations to be conducted at more rapid rotation rates and buoyancy forcing (as measured by the Ekman number Ek and Rayleigh number Ra respectively) than in conventional direct numerical simulations (DNS). We have performed 107 simulations spanning the ranges $E = 10^{-4} - 10^{-7}$ and $Ra = 10^6 - 7 \times 10^{10}$ and directly compared HD and DNS heat transfer (measured by the Nusselt number Nu), flow speeds Pe , force balances and boundary layer thicknesses. We identify two different effects of HD that are particularly clear when k_0 is below the dominant scale of the flow, k_\perp : at low supercriticality \widetilde{Ra} , Nu and Pe are increased compared to DNS due to a weakening of the rotational constraint; at high \widetilde{Ra} , Nu and Pe are decreased compared to DNS owing to suppression of energy at scales $> k_\perp$. The thermal boundary layer thickness changes in proportion to Nu , while the mechanical boundary layer thickness is marginally affected because it is determined by a vertical balance, whereas HD is applied horizontally. Heat transfer diagnostics are more strongly affected by HD than flow diagnostics, while changing k_0 has a greater impact on solution behaviour than changing q over the range of values studied. For all HD simulations with $k_0 \geq 3k_\perp$, all diagnostics remain within the standard deviation of the DNS.

I. INTRODUCTION

Rotating convection-driven flows are ubiquitous throughout the natural world. These flows are thought to be integral to the formation of magnetic fields in stars and planets [1, 2], the atmospheres of celestial bodies [3], and flows within Earth's oceans [4]. The addition of rotation into a convective flow introduces anisotropy by constraining the flow variations parallel to the axis of rotation [5–7]. This affects all global properties of the flow, including boundary layer thicknesses, heat transfer, flow speeds, energy and force balances.

The motivation for this work is to understand the dynamics of the Earth's liquid outer core, which gives rise to a magnetic field through dynamo action. Despite its proximity, the

* A footnote to the article title

† scbd@leeds.ac.uk

Earth’s core remains poorly understood due to the impracticality of direct observation and must be analysed experimentally, theoretically and numerically. Self-consistent simulations of the geodynamo have been conducted for nearly three decades [2], but due to computational limitations the viscous and thermal diffusivities must be increased by many orders of magnitude compared with their molecular values. Attempting to simulate Earth’s core dynamics with realistic parameters would result in prohibitively long run-times [8] owing to the vast range of spatial and temporal scales that need to be resolved. Fine resolution is required to resolve the small-scale structures in the flow, which necessitates small time steps. At present, the most extreme direct numerical simulations (DNS) are still orders of magnitude away from replicating the conditions found in the Earth’s outer core [e.g. 9–11]. Reaching more realistic conditions, therefore, requires numerical schemes that enable the required spatial resolution to be reduced. In this work we focus on Large Eddy Simulations (LES), which have received significant recent attention in the geodynamo literature [e.g. 12, 13]. We investigate the effect of LES in the Rotating Rayleigh-Bénard system, which allows a systematic investigation of the fundamental fluid dynamics in the regime of rapid rotation that is thought to characterise planetary cores.

A. Large-eddy simulations (LES)

The LES method effectively applies a low-pass filter to the governing fluid dynamical equations, eliminating scales smaller than the grid size. This filtering process generates equations for features larger than the grid size, which depend on a subgrid-scale (SGS) term that accounts for the interactions between the unresolved and resolved scales. One representation of the SGS term is an eddy diffusivity [14], ν_t . Multiple approaches for calculating ν_t have been proposed [e.g 15]. Regardless of the magnitude of ν_t , a shortcoming of the eddy-viscosity method is the inherent lack of scale separation. Due to their comparable size, the unresolved SGS eddies will have the largest impact on the smallest resolved eddies in the flow. Therefore, increasing diffusion at all scales doesn’t align with the anticipated physical behaviour.

A variant of these eddy-viscosity methods is hyperdiffusion (HD). In this method, the SGS processes are accounted for by changing the standard diffusion term in the governing equations. The diffusion term can be modified by increasing the order of the derivative,

which has the effect of enhancing diffusion at smaller scales [16]. Alternatively, the diffusion term can be multiplied by a function that is dependent on length scale [17–19]. A benefit of this “scale-dependent” HD scheme is the flexibility in selecting the function so that it can be customised to suit the problem. Although HD struggles to accurately model anisotropic turbulence found in planetary cores [20], this flexibility in function selection enables the adjustment of parameters to preserve the large scales.

The similarity model is a method that uses the large scale flow to control the behaviour of the SGS term [21]. In this approach, the energy exchange resulting from the interaction with the SGS eddies is approximated by the energy transfer from the smallest resolved scales. This model has the advantage of being able to accurately capture anisotropic turbulence. However, it requires adding an additional term for non-uniform grids due to commutation errors found at the boundaries [22, 23]. Furthermore, essential to the method are coefficients which depend both on space and time [24, 25]. Although the similarity method is better equipped to model anisotropic turbulence than HD and the eddy-viscosity models [20], these added complications make the method more difficult to implement.

Recent geodynamo simulations have employed a scale-dependent HD scheme based on the spherical harmonic representation of scalar fields in spherical geometry [13, 19]. This method is straightforward to implement and allows explicit control of the scales that are influenced by HD. Initial comparisons with DNS are promising [13, 19]; however, systematic comparisons have yet to be performed. Here we perform such a comparison within the framework of Rotating Rayleigh–Bénard convection.

B. Rotating Rayleigh–Bénard convection

The classic framework for studying convective flows is rotating Rayleigh–Bénard convection (RRBC). Within this framework, a plane layer of fluid is heated from below and rotated around a central axis. The fluid density is assumed to be constant other than in the buoyancy term (the Boussinesq approximation) [26]. This simplified system still captures the interaction between rotation and convection but allows more extreme parameters to be accessed compared to the spherical shell geometry that characterises geophysical systems. In RRBC, the Rayleigh number (Ra) measures the ratio of buoyant forcing compared with dissipation, the Ekman number (Ek) is the ratio of viscosity to rotation, and the Prandtl

number (Pr) is the ratio of viscous to thermal dissipation. The behaviour of the system is often characterised by relationships of the form $\sim Ra^\alpha Ek^\beta Pr^\gamma$ for the heat transfer as measured by the Nusselt number (Nu), the typical flow speed given by the Reynolds number (Re), and the typical dimensionless flow length scale $\ell = L_\perp/L_\parallel$ where L_\perp is dominant horizontal length scale and L_\parallel is the dominant vertical length scale.

Broadly speaking, the dynamics of RRBC can be separated into weakly rotating and rapidly rotating regimes. In the weakly rotating regime, which occurs at high supercriticality, the influence of rotation is subdominant and the system exhibits scaling behaviour similar to classical RBC, with $Nu \sim Ra^{1/3}$, $Re \sim Pr^{-1/2} Ra^{1/2}$ and $\ell \sim Re^{-1/2}$ [e.g. 27]. The transition to the rapidly rotating regime occurs as Ra is decreased at fixed Ek and Pr . The value of Ra at which the transition occurs is still debated; however, it probably depends on Ek and Pr , for example as $Ek^{-8/5} Pr^{3/5}$ [28] or $Ek^{-2} Pr$ [29]. In this paper we are interested in the rapidly rotating regime as this is thought to be most relevant for planetary cores [30, 31]. We focus on the aspects of the system behaviour that will be important for identifying the influence of hyperdiffusion and refer the reader to Ecke and Shishkina [32] for a recent detailed review of RRBC.

Rotation inhibits vertical heat transfer and delays the onset of convection. In the limit of small Ek and for $Pr > 0.68$ the critical Rayleigh number Ra_c determining the onset of convective motion is given by $Ra_c \approx 8.7 Ek^{-4/3}$ [33]. As such, Ra_c increases significantly as Ek is decreased, and it is often useful to utilise $\widetilde{Ra} = Ra/Ra_c$ when comparing flows at different Ek . The nonlinear regime has been investigated using DNS [e.g. 34, 35], experiments [e.g. 36, 37], and asymptotically reduced models [e.g. 28, 38, 39]. These studies have found a variety of flow structures ranging from regular cells to geostrophic turbulence [34, 35]. These flows are characterised by a primary balance between the Coriolis force and the pressure gradient [35]. The important dynamical differences are found in the secondary force balance.

At asymptotically low Ek , theoretical studies suggest that there exists a range of Ra within the rapidly rotating regime where the system exhibits diffusion-free behaviour. In this case the secondary dynamical balance in the bulk is between ageostrophic Coriolis (C), Archimedian buoyancy (A), and inertial (I) forces (CIA) balance, which yields the scaling relations $Re \sim Ra Ek/Pr$ and $\ell \sim (Ra/Pr)^{1/2} Ek = Ro^{1/2}$ where Ro is the Rossby number [40]. Assuming a balance between mean and fluctuating thermal advection in the bulk leads

to the scaling $Nu \sim (Ra^{3/2}/Pr^{1/2})Ek^2$ [40]. These scalings have recently been found in DNS at very low $Ek \lesssim 10^{-8}$ [41]. However, owing to computational expense the majority of DNS studies of RRBC, including those presented here, are conducted at higher $Ek \gtrsim 10^{-7}$ where viscosity remains dynamically significant even at high \widetilde{Ra} . Guzmán *et al.* [35] found a secondary balance between viscosity (V), buoyancy (A), and the ageostrophic Coriolis force (C) in the bulk for $\widetilde{Ra} < 6$, the so-called VAC balance. This balance implies that $\ell \sim Ek^{1/3}$ and $Re \sim PrRaEk$. A balance between the Coriolis force and viscosity is present in the boundaries, resulting in a scaling of $\delta_v \sim Ek^{1/2}$, where δ_v is the thickness of the viscous boundary layer [42]. Using the assumption that rotation stabilises the thermal boundary layer (TBL) and that the temperature drop occurs only in the TBLs results in $Nu \sim \widetilde{Ra}^3$ [43]. This exponent has been found in DNS conducted at extreme parameter values [41]. As Ra increases, inertia enters the secondary balance [35].

C. This study

Hyperdiffusion has been used in several previous studies of the geodynamo process [13, 19, 44–49]. However, only a handful of direct comparisons between DNS and the HD solutions have been conducted, in part because of the computational costs of solving the dynamo equations in the rapidly rotating regime. For the scale-dependent horizontal HD function used in this study, Aubert *et al.* [19] and Aubert [13] compared DNS and HD for 4 different combinations of control parameters and found satisfactory agreement when considering a wide range of system diagnostics. Moreover, the effect of HD in RRBC is not well studied. In this paper, we systematically study the effect of scale-dependent horizontal HD in RRBC, which is computationally cheaper than the full dynamo problem and allows a systematic investigation across a broad range of parameter space. We present 107 simulations spanning the parameters ranges $Ek = 10^{-4} - 10^{-7}$ and $Ra = 10^6 - 7 \times 10^{10}$ for $Pr = 7$, and assess the effect of HD on heat transfer, flow speeds, force balances, energy balances, boundary layer thicknesses, and length scales.

The remainder of this paper is set out as follows. In §2, the governing equations of RRBC, output parameters, and relevant theoretical results are presented. In §3 we consider two cases in depth, the first is a solution with Ra just above Ra_c and the second is a solution with Ra roughly at the transition between rapidly rotating and weakly rotating

convection. In §4, the performance increase gained from using HD is investigated along with some guidelines for choosing the HD scheme. Knowledge acquired from the initial parameter sweep at $Ek = 10^{-5}$ is then tested at lower Ek . Finally, in §5, we present our conclusions.

II. THEORY

A. Problem formulation

We consider a Cartesian domain defined by spatial coordinates x , y , and z . The system of equations consists of the non-dimensional momentum equation, the incompressible continuity equation, and the temperature equation. We employ the simplest form of the Oberbeck-Boussinesq approximation [26, 50] whereby all fluid properties are assumed to be constant except that the density ρ in the buoyancy term depends linearly on temperature T as $\rho = \rho_0(1 - \alpha(T - T_0))$, where T_0 is the base state temperature profile, ρ_0 is the baseline density and α is the thermal expansion coefficient. The base state is in hydrostatic balance, and we consider perturbations from this base state with temperature given by $T = T_0 + \theta$. The rotation vector $\mathbf{\Omega} = \Omega \hat{\mathbf{z}}$ is parallel to the unit vector $\hat{\mathbf{z}}$, and gravity is given by $\mathbf{g} = -g\hat{\mathbf{z}}$. At the top and bottom boundaries (located at $z = \pm 0.5$), no-slip boundary conditions are applied to the velocity field, and isothermal conditions are applied to the temperature field; the sidewalls are periodic in all fields. The top and bottom boundaries are separated by a distance L and maintain a temperature difference of ΔT . The fundamental time-scale is taken to be the thermal diffusion time scale $\tau = L^2/\kappa$, \mathbf{v} is scaled by κ/L where κ is the thermal diffusivity, and the reduced pressure P by $\rho_0\kappa^2/L^2$, resulting in

$$\frac{\partial \mathbf{v}}{\partial t} + \underbrace{(\mathbf{v} \cdot \nabla) \mathbf{v}}_{\text{Inertia}} + \frac{Pr}{Ek} \underbrace{\hat{\mathbf{z}} \times \mathbf{v}}_{\text{Coriolis}} = \underbrace{-\nabla P}_{\text{Pressure}} + \underbrace{Pr \nabla^2 \mathbf{v}}_{\text{Diffusion}} + \underbrace{Ra Pr \theta \hat{\mathbf{z}}}_{\text{Buoyancy}}, \quad (1)$$

$$\nabla \cdot \mathbf{v} = 0, \quad (2)$$

$$\frac{\partial \theta}{\partial t} + (\mathbf{v} \cdot \nabla) \theta = w + \nabla^2 \theta, \quad (3)$$

where t is time. The Rayleigh number Ra , Prandtl number Pr and Ekman number Ek are defined as,

$$Ra = \frac{g\alpha\Delta TL^3}{\nu\kappa}, \quad Pr = \frac{\nu}{\kappa}, \quad Ek = \frac{\nu}{2\Omega L^2}, \quad (4)$$

where ν is the kinematic diffusivity.

Simulations are conducted using the open source pseudospectral code Dedalus [51]. The solution is represented by Fourier modes in the x and y directions and Chebyshev polynomials in the z direction. The Chebyshev grid has collocation points clustered near the boundaries, allowing for adequate resolution for the boundary layers [51]. The use of Fourier modes guarantees periodic boundary conditions at the horizontal boundaries. The spatial resolution of each simulation is described by the number of collocation points N_x, N_y, N_z in the x, y, z directions respectively. Time stepping is carried out using a 4th-order Runge-Kutta scheme; linear terms are treated implicitly, and non-linear terms explicitly. Dedalus utilises a pseudo-spectral method such that the non-linear terms are computed in grid space and the linear terms in coefficient space. The aspect ratio of the box, denoted as Γ , is varied from 0.5 to 4. To capture the convective dynamics adequately, a minimum of 10 convective cells is ensured in all simulations.

B. Output parameters

We calculate several flow diagnostics to understand the global properties of each simulation. The integral Nusselt number Nu_I is

$$Nu_I = \frac{1}{\Gamma^2} \int_{-0.5}^{0.5} \int_0^\Gamma \int_0^\Gamma \left(w\theta - \frac{\partial\theta}{\partial z} \right) dx dy dz. \quad (5)$$

Flow speeds are quantified by the Péclet number (Pe), calculated as

$$Pe = \frac{1}{\Gamma^2} \int_{-0.5}^{0.5} \int_0^\Gamma \int_0^\Gamma \sqrt{\mathbf{v} \cdot \mathbf{v}} dx dy dz, \quad (6)$$

and the Reynolds number Re is given by $Re = PePr$. The thickness of the thermal boundary layer δ_T is calculated by taking the location of the peak of the horizontally averaged root mean square (r.m.s) of the thermal perturbation field [52] given by

$$\theta_{rms}(z) = \overline{\left\langle \sqrt{(\theta - \langle \theta \rangle_H)^2} \right\rangle_H}, \quad (7)$$

where $\langle \rangle_H$ refers to an average along the horizontal coordinates and an overbar refers to a time average. The viscous boundary layer thickness δ_v is calculated using the peak of the horizontally averaged velocity field [53],

$$U_h = \sqrt{\langle \mathbf{v} \cdot \mathbf{v} \rangle_H}. \quad (8)$$

217

218 To check convergence, we use the fact that the time-averaged kinetic energy equation
 219 yields an exact balance between the viscous dissipation V_d and the buoyant production B_p
 220 [54], where

$$221 \quad V_d = \frac{Pr}{\Gamma^2} \int_{-0.5}^{0.5} \int_0^\Gamma \int_0^\Gamma \mathbf{v} \cdot \nabla^2 \mathbf{v} \, dx dy dz, \quad (9)$$

222

$$223 \quad B_p = \frac{RaPr}{\Gamma^2} \int_{-0.5}^{0.5} \int_0^\Gamma \int_0^\Gamma \theta w \, dx dy dz. \quad (10)$$

224 A balance within 1% between the time average of each quantity, denoted as E_b and given
 225 by

$$226 \quad E_b = \frac{\overline{V_d} - \overline{B_p}}{\overline{V_d}}, \quad (11)$$

227 is used to show statistical convergence. A further convergence check is provided by comparing
 228 the Nusselt number evaluated as an integral over the volume (equation 5) and the Nusselt
 229 number Nu_t (Nu_b) evaluated at the top (bottom) of the domain, where

$$230 \quad Nu_t = \frac{1}{\Gamma^2} \int_0^\Gamma \int_0^\Gamma \left. \frac{\partial \theta}{\partial z} \right|_{z=0.5}, \quad (12)$$

231

$$232 \quad Nu_b = \frac{1}{\Gamma^2} \int_0^\Gamma \int_0^\Gamma \left. \frac{\partial \theta}{\partial z} \right|_{z=-0.5}. \quad (13)$$

233 Conservation of energy requires that $\overline{Nu_t} = \overline{Nu_b} = \overline{Nu_I}$ [43]. A tolerance of 1% in the
 234 maximum error is used to further show convergence (a summary of all runs is shown in
 235 appendix A).

236 Adequate spatial resolution was ensured by conducting several runs at $Ek = 10^{-5}$, $Ra =$
 237 7.00×10^7 , $Pr = 7$, and $\Gamma = 1$. Runs were conducted with a resolution (N_x, N_y, N_z) of
 238 $(64, 64, 64)$, $(128, 128, 64)$, $(128, 128, 128)$ and $(192, 192, 128)$. In all cases Nu_I , Nu_t and Nu_b
 239 agreed with one another to a tolerance of less than 1%, and the resolution of $(128, 128, 128)$
 240 was used for all remaining DNS at $Ek = 10^{-5}$. However, to ensure 10+ convective cells are
 241 present in each simulation, Γ is adjusted for each Ek . N_z is also adjusted to ensure at least
 242 7 points are within each boundary layer.

243 1. Force balances & length scales

244 Previous studies have assessed force balances in a number of different ways. These include
 245 calculating forces at the mid-plane [35], as a function of wavenumber [19], or using projected

forces that remove gradient contributions [55]. Another possibility is to use the vorticity balance [56, 57], which also removes the dynamically irrelevant gradient components of each force while being easier to compute than the projection method. Here we use the vorticity balance, obtained by taking the curl of each force, which yields the following terms [57]:

$$\boldsymbol{\omega}_I = (\boldsymbol{\omega} \cdot \nabla) \mathbf{v} - (\mathbf{v} \cdot \nabla) \boldsymbol{\omega}, \quad \boldsymbol{\omega}_C = -\frac{Pr}{Ek} \frac{\partial \mathbf{v}}{\partial z}, \quad (14)$$

$$\boldsymbol{\omega}_v = Pr \nabla^2 \boldsymbol{\omega}, \quad \boldsymbol{\omega}_B = Ra Pr \left(\frac{\partial \theta}{\partial y}, \frac{\partial \theta}{\partial x}, 0 \right).$$

We have analysed the vorticity terms in two ways. First we calculate integrated squared vorticity terms over the bulk domain. We found that a robust estimate of the bulk balance required removing regions of size $2\delta_v$ adjacent to the top and bottom boundaries, i.e. twice the viscous boundary layer thickness, and this is the definition of the bulk domain used throughout. Second, we compute the horizontal length scale dependence of each vorticity term. For a quantity $A = (a_x, a_y, a_z)$, we take Fourier transforms in x and y , multiply by the complex conjugate of each component, add these products together and integrate over z (excluding the boundary layers) to obtain

$$a(k_x, k_y) = \int_{-0.5+2\delta_v}^{0.5-2\delta_v} [\mathcal{F}(a_x) * \mathcal{F}(a_x) + \mathcal{F}(a_y) * \mathcal{F}(a_y) + \mathcal{F}(a_z) * \mathcal{F}(a_z)] dz. \quad (15)$$

We then sum over shells in the (k_x, k_y) plane where shell n is defined by wavenumbers which satisfy $k_{n-1} < k_h < k_n$ where $k_h = \sqrt{k_x^2 + k_y^2}$ is the horizontal wavenumber.

A final important quantity in the analysis of HD is the dominant horizontal flow length scale $L_\perp = 2\pi/k_\perp$. We estimate k_\perp using the peak in the kinetic energy spectrum obtained from equation (15).

C. Scaling in RRBC

1. Length scales

All simulations reported in this paper exhibit a leading order geostrophic force balance, given by

$$\hat{\mathbf{z}} \times \mathbf{v} \sim -\nabla P. \quad (16)$$

Taking the curl of both sides yields

$$\nabla \times (\hat{\mathbf{z}} \times \mathbf{v}) \sim \mathbf{0}, \quad (17)$$

from which follows $\frac{\partial \mathbf{v}}{\partial z} \sim \mathbf{0}$ which is the Taylor-Proudman (TP) constraint and shows that the flow will be largely invariant in z [5, 6]. This invariance in z can be formalised by defining the horizontal (L_\perp) and vertical length scales (L_\parallel). Horizontal derivatives are associated with L_\perp and vertical derivatives with $L_\parallel \sim L$.

The TP constraint must be broken to sustain convective motion, and other forces must enter the force balance. When the TP constraint is broken by viscosity, the vorticity balance can be estimated as

$$\frac{2\Omega V}{L_\parallel} \sim \frac{\nu V}{L_\perp^3} \quad (18)$$

where V is the typical scale of velocity. It follows from (18) that [e.g. 58]

$$\ell = \frac{L_\perp}{L_\parallel} \sim Ek^{1/3}. \quad (19)$$

At higher Ra , inertia can become important in the vorticity balance. Assuming a balance between rotation and inertia gives

$$\frac{2\Omega V}{L_\parallel} \sim \frac{V^2}{L_\perp^2} \quad (20)$$

and hence

$$\ell = \frac{L_\perp}{L_\parallel} \sim Ro^{1/2}, \quad (21)$$

where $Ro = V/2\Omega L$ is the Rossby number.

2. Heat transfer and thermal boundary layers

Scaling relations for Nu and δ_T differ depending on whether the boundary layers or the bulk throttle the heat transport. In the rotationally dominated regime, scaling theories for Nu begin with the assumption that rotation stabilises the TBL. It is also assumed that most of the temperature drop occurs within the TBL and that heat is primarily transferred by conduction across the TBL. From this, a scaling is derived for both the TBL thickness and Nu [43], given by

$$\delta_T \sim Ra^{-3}, \quad (22)$$

$$Nu \sim 0.0023 Ra^3 Ek^4. \quad (23)$$

In rotationally affected regimes, a scaling theory for Nu is derived by assuming that the heat flux q is diffusionless. Stevenson [59] and Julien *et al.* [28] show that the only combination of parameters which satisfy this assumption are

$$Nu - 1 \sim \frac{Ra^{3/2} Ek^2}{Pr^{1/2}}. \quad (24)$$

3. Flow speeds

Taking the scalar product of equation (1) with \mathbf{v} and integrating over space and time leads to [27, 54, 60]

$$\nu \langle (\nabla \mathbf{v})^2 \rangle_V = \frac{\nu^3}{L_{\parallel}^4} \frac{Ra(Nu - 1)}{Pr^2}. \quad (25)$$

where $\langle \cdot \rangle_v$ is a volume average. In the rotationally dominated regime where the VAC balance is thought to hold, equation (19) is used to get

$$Pe_{VAC} = Ek^{1/3} Ra^{1/2} (Nu - 1)^{1/2}. \quad (26)$$

In the rotationally affected regime where we expect the CIA force balance to hold, a scaling law for flow speeds is derived by first balancing the inertia and buoyancy terms in the energy equation, giving

$$\frac{V^3}{L_{\perp}} \sim \frac{\nu^3}{L_{\parallel}} \frac{Ra(Nu - 1)}{Pr^2}. \quad (27)$$

Combining this with (21) yields [61]

$$Pe_{IAC} = Ra^{2/5} Ek^{1/5} (Nu - 1)^{2/5} Pr^{1/5}. \quad (28)$$

Combining this with the scaling for Nu in the CIA regime [equation (24)] gives

$$Pe_{IAC} \sim Ra Ek. \quad (29)$$

4. Mechanical boundary layers

In the rotationally dominated and rotationally affected regimes, the dominant force balance in the boundary layer is between the pressure gradient, Coriolis force and the viscous force, given by

$$\nabla P \sim 2\mathbf{\Omega} \times \mathbf{v} \sim \nu \nabla^2 \mathbf{v}. \quad (30)$$

The dominant term in the Laplacian is the vertical derivative and is of order $\nu V/\delta_v^2$, which implies that [42]

$$\delta_v/L_{||} \sim Ek^{1/2}. \quad (31)$$

D. Form of the Hyperdiffusion Function

We follow Nataf and Schaeffer [12] and choose a function with two variables: a cutoff wavenumber k_0 and a growth rate q . The function is defined as

$$f(k) = \begin{cases} 1, & \text{for } k < k_0 \\ q^{k-k_0}, & \text{otherwise.} \end{cases}$$

Each second-order derivative in the diffusion term is multiplied by a function which depends on the wavenumber of that derivative. However, so as not to directly affect boundary layers in the problem, the z derivative is excluded. As such, the horizontal diffusion operator is given by

$$\nabla_H^2 = f(k_x)k_x^2 + f(k_y)k_y^2 \quad (32)$$

HD is applied only to the velocity field to damp small-scale motion; although it could equally be applied to the temperature field, we have chosen not to in order to clearly isolate its effect on the flow, with the thermal case offering an interesting avenue for future work. Other forms of HD could have been used, for example the horizontally isotropic form $\sqrt{(k_x^2 + k_y^2) \times (k_x^2 + k_y^2)}$.

As explained in section 2.2.1, L_{\perp} is an important length scale as this is the length scale that contains the most energy. Given that L_{\perp} can be predicted from scaling theories, this can be used to construct HD schemes (via the selection of k_0) that do not affect the most important scales. In principle, an upper value on q could be chosen such that the ordering of forces at any scale is left unchanged. However, this cannot be chosen *a priori* but rather from empirical evidence from previous runs.

III. RESULTS

Figure 1 shows the four contributions to the vorticity balance in our DNS runs for all Ra at $Ek = 10^{-5}$ (a) and 10^{-7} (b). The general balances and ordering of terms is compatible with

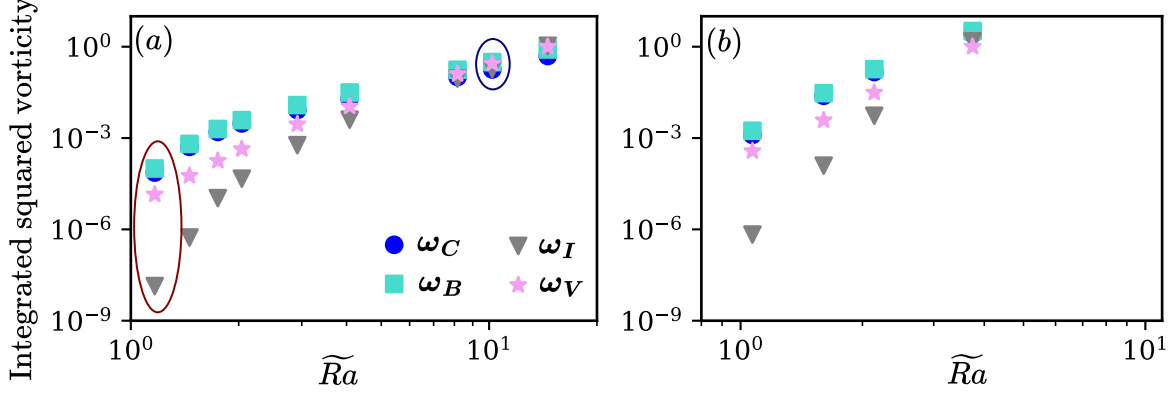


FIG. 1. The integrated squared vorticity contributions for all DNS runs conducted at (a) $Ek = 10^{-5}$, (b) $Ek = 10^{-7}$.

the results of Guzmán *et al.* [35], who analysed forces at the midplane of a cartesian domain. At low \widetilde{Ra} , the dominant balance is VAC with the inertial term strongly subdominant, as found by Guzmán *et al.* [35] in their “Cells” and “Columns” regimes. The inertial term increases with increasing \widetilde{Ra} and eventually reaches the same order as the remaining terms, creating an IVAC balance as in the “Plumes” regime of Guzmán *et al.* [35]. Since we focus on vorticity contributions (over momentum terms), we find the diffusion term to be larger when compared to other terms. This is to be expected as taking the curl of a quantity disproportionately increases terms which are larger at smaller scales.

Figure 2 shows Nu_I , Pe , δ_v , δ_T , and ℓ for all DNS runs in this study. Also shown is the ratio ω_I/ω_C , which characterises the dominant vorticity balance in our simulations (see Figure 1). At relatively low \widetilde{Ra} the scalings of all quantities are consistent with theoretical predictions for the VAC balance (Section III A). For Nu there is no evidence of the diffusion-free scaling $Nu \sim (Ra/Ra_c)^{3/2}$ as expected given the values of Ek considered. The dominant flow length scale shows a clear $Ek^{1/3}$ dependence (Figure 2f), with some deviation from the behaviour as Ra increases. At the highest values of Ra considered, the scaling behaviour of all quantities changes, which is consistent with the change in the dominant vorticity balance (Figure 2d). The spatial resolution of each run was determined by considering the peak-to-trough drop-off in the kinetic energy spectrum and the temperature field spectrum plotted as a function of k_h . For all runs, both fields were resolved sufficiently with at least two orders of magnitude drop-off between peak and trough.

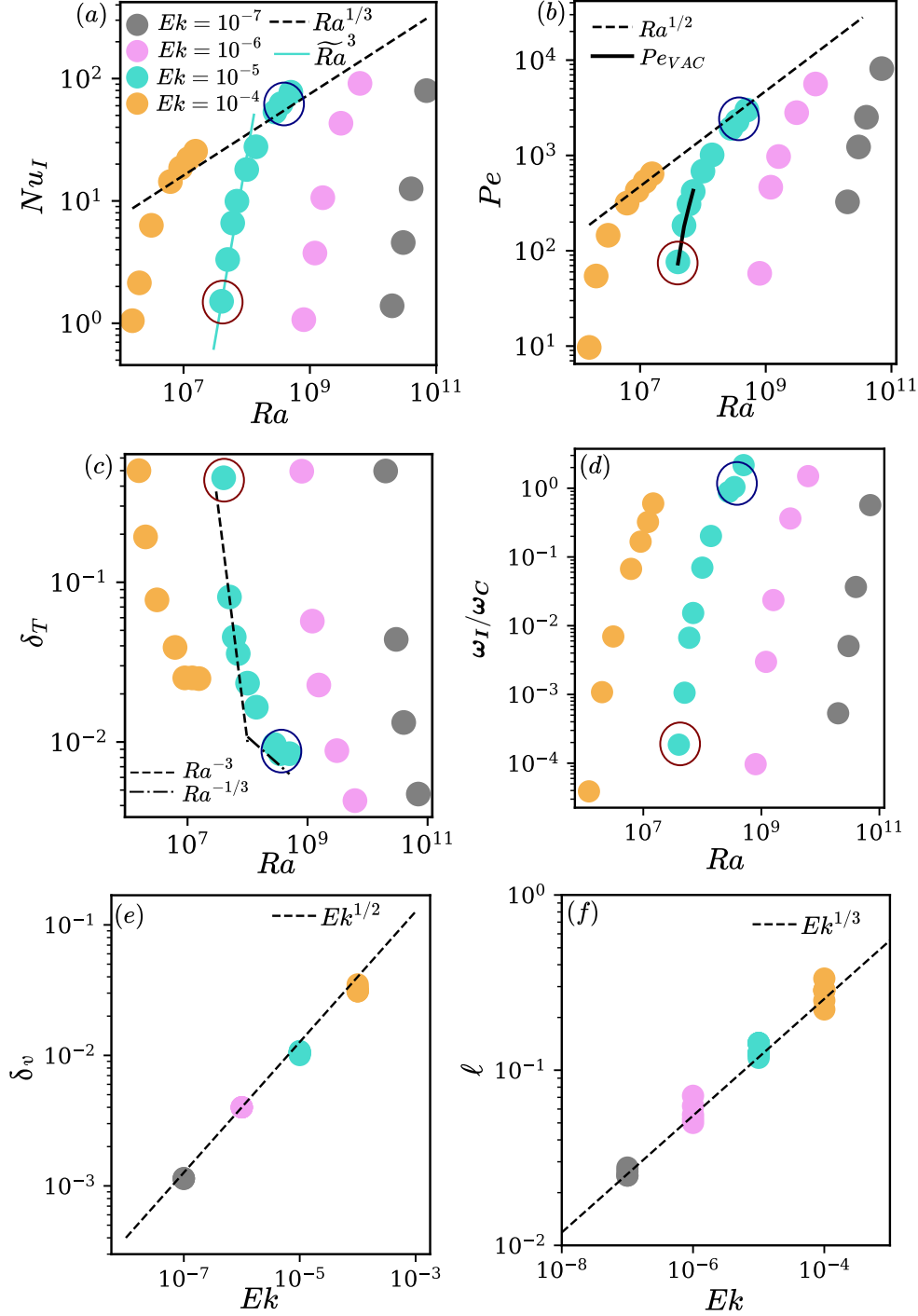


FIG. 2. (a) The Nusselt number as a function of Ra and coloured by Ek , with scaling laws: $Nu \sim \widetilde{Ra}^3$ [43] and $Ra^{1/3}$ [62]. (b) The Péclet number as a function of Ra and coloured by Ek , with a best-fit scaling law of $Ra^{1/2}$ [60], the black line shows Pe_{VAC} (equation (26)). (c) The thermal boundary layer, with scalings from classical TBL theory [43, 62]. (d) The ratio of the integrated squared inertia vorticity term to the integrated squared vorticity Coriolis term. (e) The viscous boundary layer thickness as a function of Ek , with a $1/2$ scaling law [42]. (f) The convective length scale as a function of Ek with the VAC scaling (equation (18)).

We begin by examining in detail the two cases circled in Figures 1 and 2. The red circled case, discussed in section III A, corresponds to the cellular regime of Guzmán *et al.* [35] and is in VAC balance. The blue case, discussed in section III B, is in the plumes regime of Guzmán *et al.* [35] and is in IVAC balance. In section III C we then consider the effect of HD as a function of Ra and Ek before evaluating the effect of changing the growth factor q . Finally, we consider the computational gains of using HD in section III E.

A. Example Solution in VAC Balance

We consider the solution with $Ek = 10^{-5}$, $\widetilde{Ra} = 1.16$, $Pr = 7$ and $\Gamma = 2$, which is in VAC balance. At these conditions $k_{\perp} = 17$ and so we ran 4 HD runs with $k_0 = 8, 16, 32, 48$ in equation 32, which are close to multiples of k_{\perp} and set $q = 1.05$.

Table III shows Nu_I , Pe , δ_v , δ_T , V_d , L_{\perp} and E_b for all runs conducted with $q = 1.05$; the cases considered in this section are highlighted in bold and indicated with a *. For $k_0 \geq 16$, both Nu_I and Pe remain within the standard deviation of the DNS; however, when $k_0 = 8$, both values exceed the DNS. Figure 3(a-b) shows Nu_I and Pe plotted against convective overturn time, given by $t \times Pe$, and shows that the $k_0 = 8$ case never overlaps with the DNS at any t and has greater variability. Figure 3(c-d) shows vertical profiles of U_h and θ_{rms} . The increased kinetic energy for $k_0 = 8$ is again apparent and there is greater vertical variation in U_h for this case. For θ_{rms} there is also a clear change in δ_T . This is not the case for δ_v ; although the profile of U_h is changed, the location of the peak of the profile is not. Figure 4 shows the vertically integrated \hat{z} component of velocity for the DNS case (a), the $k_0 = 32$ case (b) and the $k_0 = 8$ case (c) and kinetic energy spectrum for difference values of k_0 (d). For $k_0 = 8$, k_{\perp} decreases from 17 to 15, and there is also more energy in the large scale modes than the DNS.

Figures 3 and 4 both demonstrate that kinetic energy is increased for the HD case with $k_0 = 8$ compared with the DNS. We argue this arises because HD with $k_0 < k_{\perp}$ weakens the influence of rotation by increasing the dominant scale of the flow. In the VAC regime $L_{\perp} \sim Ek^{1/3}$ [equation (19)] and so the decrease in k_{\perp} from the DNS value of 17 to the $k_0 = 8$ value of 15 (Figure 4d) corresponds to an effective increase in the Ekman number of the simulation [c.f. 18]. Since $Ra_c \sim Ek^{-4/3}$, increasing Ek lowers Ra_c and increases the supercriticality \widetilde{Ra} of the simulation because Ra is fixed. In the VAC regime $Nu \sim \widetilde{Ra}^3$ and

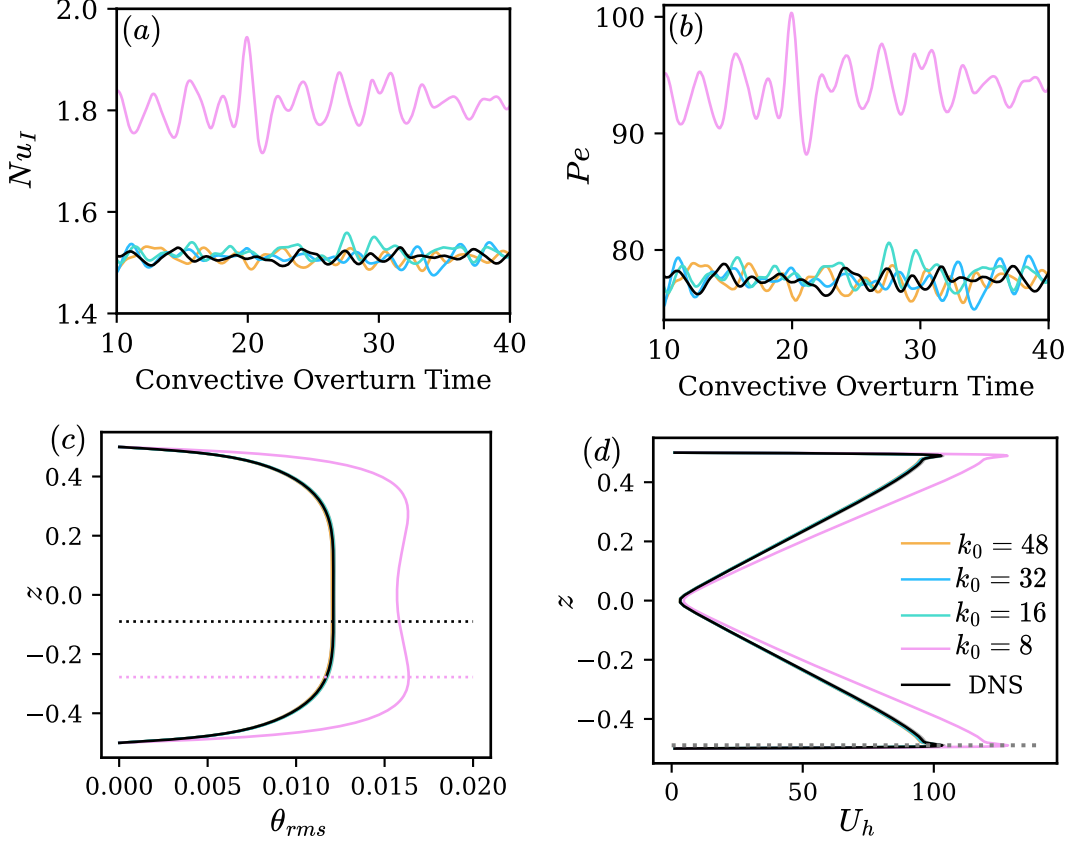


FIG. 3. (a) The integral Nusselt number plotted as a function of convective overturn time for the DNS case and 4 HD cases with a cut-off wavelength of $k_0 = 48$, $k_0 = 32$, $k_0 = 16$ and $k_0 = 8$. All cases were ran at $Ra = 4 \times 10^7$, $\widetilde{Ra} = 1.16$, $Ek = 10^{-5}$, $Pr = 7$ and $\Gamma = 2$. (b) The Péclet number is plotted as a function of convective overturn time for the same runs. (c) Vertical profile of θ_{rms} for the same runs, the dotted black line shows the peak of the DNS profile and the dotted pink line shows the peak of the HD profile with $k_0 = 8$. (d) Vertical profile of U_h for each run, the dotted grey line shows the peak of all runs.

$Pe \sim Ek^{1/3} Nu^{1/2}$, and hence both Nu and Pe are expected to increase for the $k_0 = 8$ case compared to the DNS. A weakening of the rotational constraint also implies greater vertical variation in the velocity (Figure 3). This behaviour is consistent with the simulation results in Figures 3 and 4.

To test the proposed mechanism, we conducted linear stability analysis using the Dedalus eigenvalue solver [51] to determine Ra_c and L_\perp for a DNS case and a HD case where $k_0 = 8$. In the DNS $Ra_c = 3.46 \times 10^7$ and $L_\perp = 17$, whereas in the HD case $Ra_c = 3.08 \times 10^7$ and $L_\perp = 15.28$. The DNS and HD spectrum peaks in figure 4d align well with the predicted

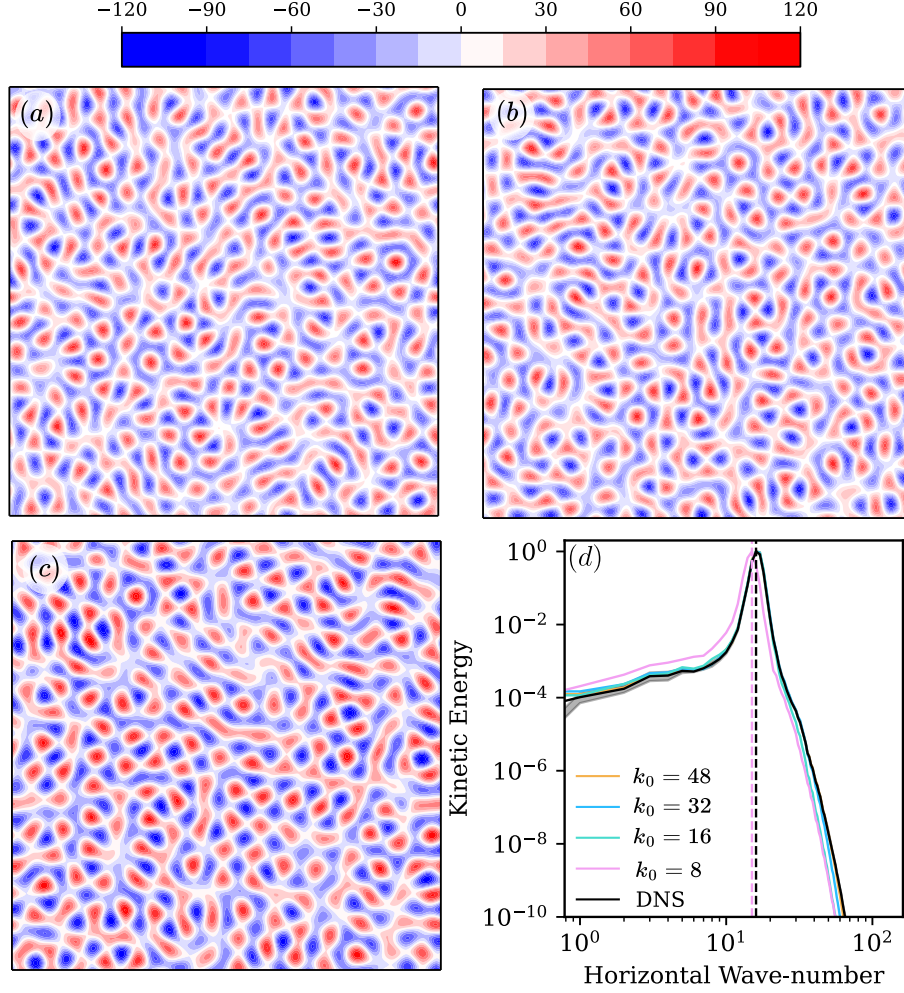


FIG. 4. (a) The integrated \hat{z} component of velocity of a run at $Ra = 4 \times 10^7$, $\widetilde{Ra} = 1.16$, $Ek = 10^{-5}$ and $\Gamma = 2$ for DNS. (b) $k_0 = 32$. (c) $k_0 = 8$. (d) The time-averaged kinetic energy spectrum of each of the runs is plotted as a function of the horizontal wave number. The dotted black line is the first unstable mode in the HD case where $k_0 = 8$ as predicted from the linear stability analysis. The solid black line is the first unstable mode in the DNS case.

peaks from the linear stability analysis. To confirm that the HD treatment has lowered Ra_c , a DNS and HD run with $k_0 = 8$ were conducted at $Ra = 3.2 \times 10^7$, which is below the DNS Ra_c for this Ek . In the HD case, convection was observed yielding solutions with $Pe > 1$ and $Nu > 1$, whereas in the DNS case, no convection was observed, reflecting the difference in Ra_c .

The vorticity balances for the DNS and HD runs are shown in figure 5. The dominant balance is between ω_C and ω_B in all runs. The viscous term becomes comparable to ω_C and

ω_B at k_\perp for each run, while at higher k the magnitude of all three terms drops dramatically. Inertia remains subdominant at all scales. Coriolis and inertial terms are most reduced in the HD runs compared with DNS. However, the reduction occurs only for $k \gg k_\perp$ at scales that make an insignificant contribution to the overall vorticity balance and therefore have a negligible effect on the flow (see figures 3 and 4). The variation of the viscous term with k is similar for all runs and does not show an increase at high k as might be expected from the form of the hyperdiffusion function (equation 32) because the increase in $f(k)$ with k is compensated by both the reduction in \mathbf{v} and increase in L_\perp . For $k_0 = 16, 32$ and 48 , the spectra at large scales ($k < k_\perp$) for all terms are only marginally perturbed from the DNS. For $k_0 = 8$ the spectra for all terms are essentially shifted towards lower wavenumber and higher amplitude; the relative ordering of terms is closely preserved even to wavenumbers far above k_\perp . Indeed, the $k_0 = 8$ spectra qualitatively resemble the spectrum of a marginally supercritical simulation at slightly higher Ek to the DNS.

The energy and vorticity spectra for the VAC simulation (Figures 4 and 5) are strongly peaked around k_\perp . Our HD simulations with $k_0 \geq 2k_\perp$ perturb the dynamics at small scales ($k \gg k_\perp$) but leave the dynamics at scales $\leq k_\perp$ largely unaltered. For $k_0 < k_\perp$ HD suppresses the most unstable mode of the DNS and a mode of larger scale is preferred instead. When interpreted as a reduction in the rotational constraint, this behaviour can explain the increase in Nu , Pe , and vertical velocity variations seen in the HD simulation compared to its DNS counterpart.

B. Example Solution in IVAC Balance

We now consider the solution with $Ek = 10^{-5}$, $\widetilde{Ra} = 10.12$, $Pr = 7$ and $\Gamma = 2$, for which $k_\perp = 13$. In this run the inertial, viscous, buoyancy and Coriolis terms are of comparable magnitude (Figure 2d) and so the force balance can be termed IVAC. We conducted 4 HD runs for these parameters using the same k_0 values as in Section III A and keep $q = 1.05$ to aid comparison.

A summary of Nu_I , Pe , δ_v , δ_T , and E_b for each of the HD runs along with the DNS run is shown with a + sign and highlighted in bold in appendix A. With $k_0 \geq 16$ both Nu and Pe remain within the standard deviation of the DNS; however, for $k_0 = 8$ both quantities are reduced below the standard deviation of the DNS run (Figure 6(a-b)). The

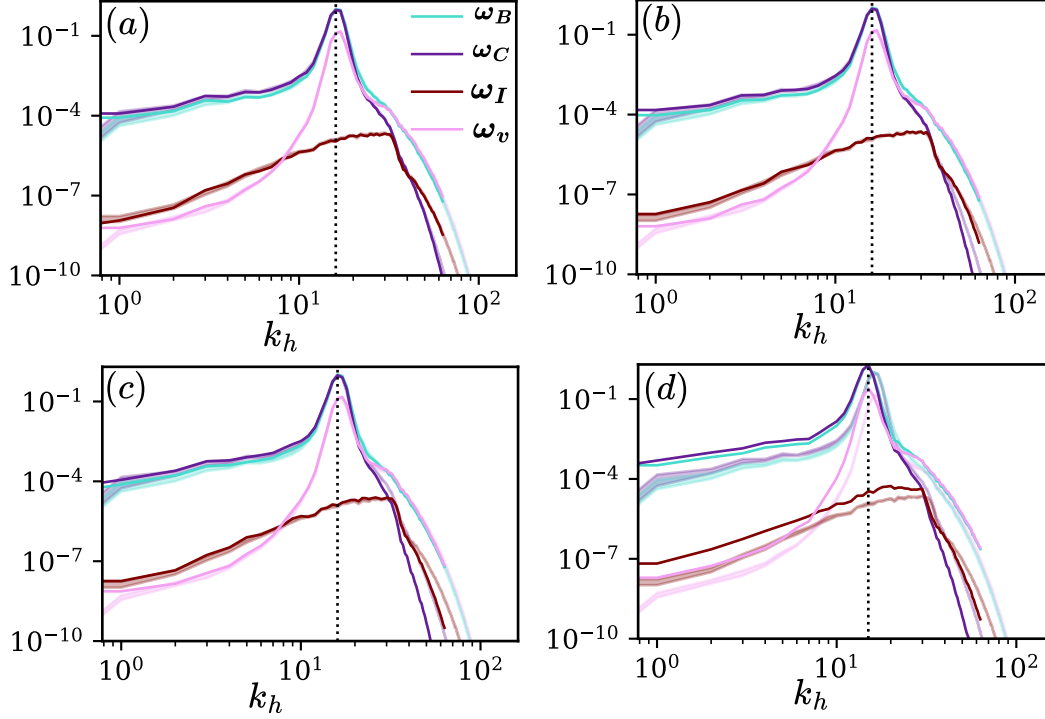


FIG. 5. Wave-number dependence of each vorticity contribution for each HD run. The shaded regions are the standard deviation surrounding the average of the DNS run at the same parameter regime. The dotted vertical line is located at k_{\perp} of the HD run. Case run at $Ra = 4 \times 10^7$, $\widetilde{Ra} = 1.16$, $Ek = 10^{-5}$, $Pr = 7$ and $\Gamma = 2$ and k_0 . (a) $k_0 = 48$, (b) $k_0 = 32$, (c) $k_0 = 16$, (d) $k_0 = 8$.

viscous boundary layer thickness remains consistent up to 4 significant figures throughout all runs. The thermal boundary layer thickens as k_0 is reduced, with a maximum increase of 14.3% for the case with $k_0 = 8$. Figure 7 shows the vertically integrated \hat{z} component of velocity and the kinetic energy spectrum for DNS and HD cases. The figure shows that each HD run contains less energy than the DNS run at the smallest resolved scale.

Figures 6 and 7 show that decreasing k_0 decreases the convective vigour of the solution. Increasing the viscous effects reduces the amplitude of the velocity fields, particularly at the small scales where $f(k)$ is the largest. Here, unlike the VAC regime, there is substantial energy in wavenumbers up to 3–4 times k_{\perp} and hence the reduction in energy at these scales can affect global quantities such as Pe . Since $Nu \sim Pe^2$ the heat transfer is also expected to decrease. The reduction in Nu and Pe is most pronounced when $k_0 = 8$. This occurs because decreasing k_0 increases the number of scales affected by the HD and also because the magnitude of $f(k)$ and hence the effect of HD at a given k increases as k_0 decreases.

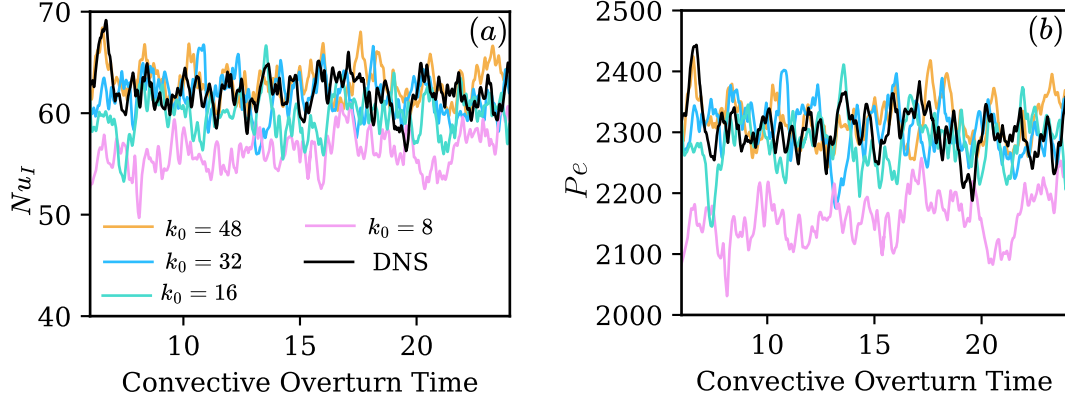


FIG. 6. (a) The integral Nusselt number plotted as a function of convective overturn time for the DNS case and 4 HD cases with a cut-off wavelength of $k_0 = 48$, $k_0 = 32$, $k_0 = 16$ and $k_0 = 8$. All cases were ran at 3.5×10^8 , $\widetilde{Ra} = 10.12$, $Ek = 10^{-5}$, $Pr = 7$ and $\Gamma = 2$ and shown an IVAC force balance. (b) The Péclet number is plotted as a function of convective overturn time for the same runs.

Figure 9 shows the vorticity balances for the DNS and each HD run. In the DNS at k_\perp the dominant balance is between Coriolis, buoyancy and inertial terms, and hence the dominant flow scale may be expected to follow the CIA scaling, equation (21). This is supported by the scaling of ℓ at high Ra in Figure 8. At higher k (≥ 40) the viscous term reaches the same magnitude as the CIA terms, which may be what gives rise to the IVAC balance seen in the integrated forces and vorticity terms (Figure 2). In the HD cases the most significant changes compared to the DNS are an increase in the viscous term and decrease in the inertial term for $k > k_\perp$. These differences get larger as k_0 decreases. Indeed, and unlike the VAC case in Section III A, at $k_0 = 8$ the HD perturbs the dominant vorticity balance for $k > k_\perp$ as inertia remains subdominant and the small-scale balance is VAC.

In this IVAC simulation the decrease in Nu and Pe with decreasing k_0 arises because the HD suppresses energy and changes the dominant balance of vorticity terms for $k > k_\perp$. The dynamics at k_\perp are relatively unaffected because they are determined by a CIA balance that is independent of diffusivities.

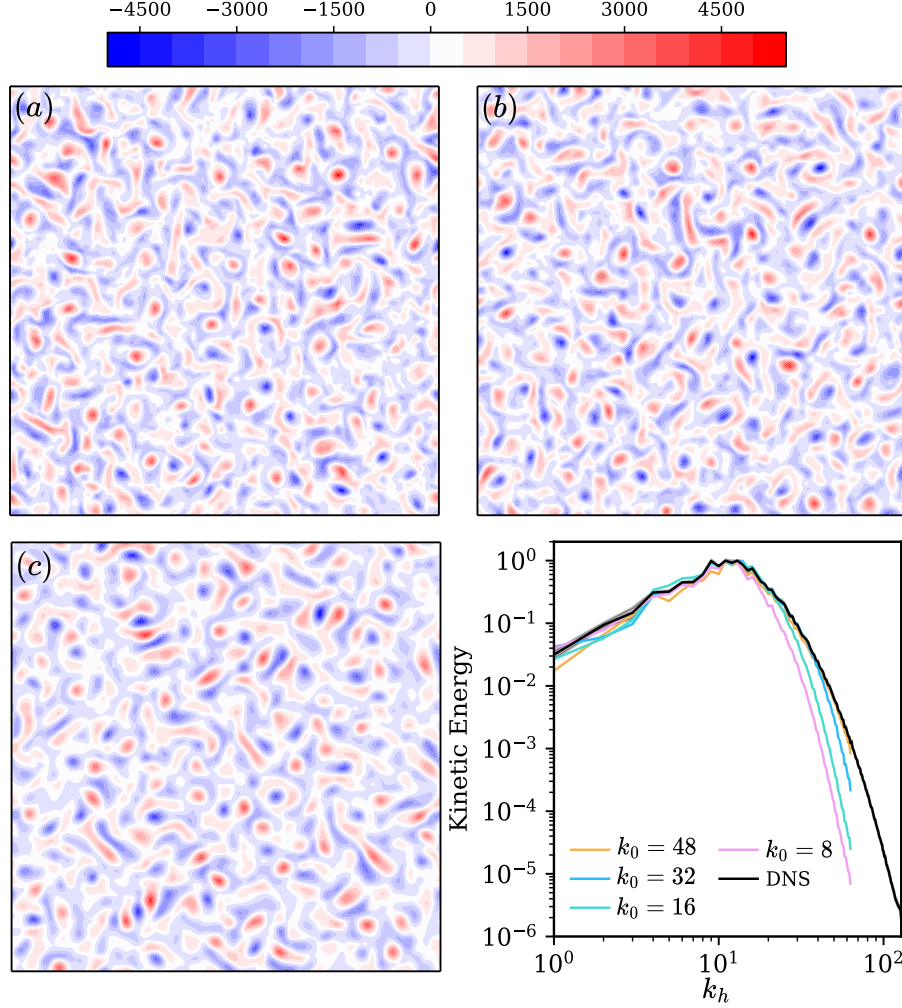


FIG. 7. (a) The integrated \hat{z} component of velocity of a run at $Ra = 3.5 \times 10^8$, $\widetilde{Ra} = 10.12$, $Ek = 10^{-5}$ and $\Gamma = 2$ for DNS in IVAC balance. (b) $k_0 = 32$. (c) $k_0 = 8$. (d) The time-averaged kinetic energy spectrum of each of the runs is plotted as a function of the horizontal wave number.

C. Scaling Behaviour of RRBC with HD

So far we have identified two different effects of HD that are particularly clear when $k_0 < k_\perp$: at low \widetilde{Ra} , Nu and Pe are increased compared to DNS due to a weakening of the rotational constraint; at high \widetilde{Ra} , Nu and Pe are decreased compared to DNS owing to a suppression of energy at scales $> k_\perp$. The thermal boundary layer thickness δ_T is altered proportionally to the change in Nu , while the mechanical boundary layer thickness δ_v is only marginally affected because it is determined by a vertical balance whereas HD is applied in the horizontal directions. We now consider the effect of HD in a series of simulations with

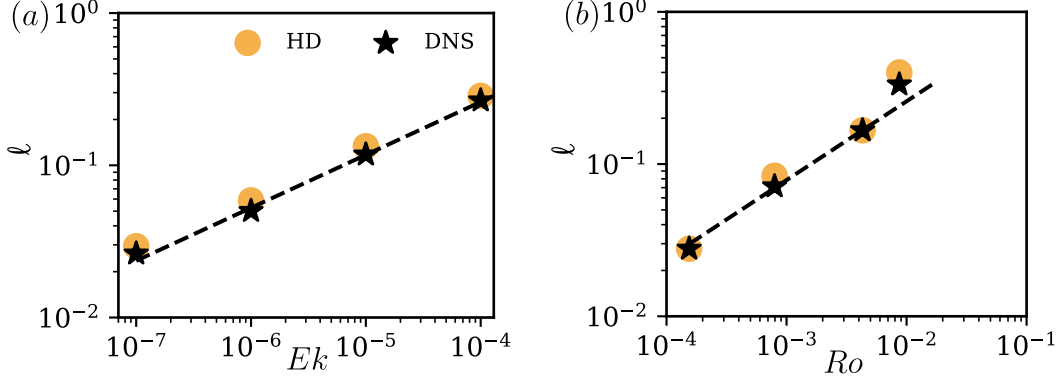


FIG. 8. (a) The perpendicular length scale plotted against the Ekman number for runs with the lowest Ra at each Ekman number. The scaling shown is a best fit line with gradient 0.35. (b) The perpendicular length scale plotted against the Rossby number for the highest Ra

conducted at each Ekman number. The scaling is a best fit line with a gradient of 0.49.

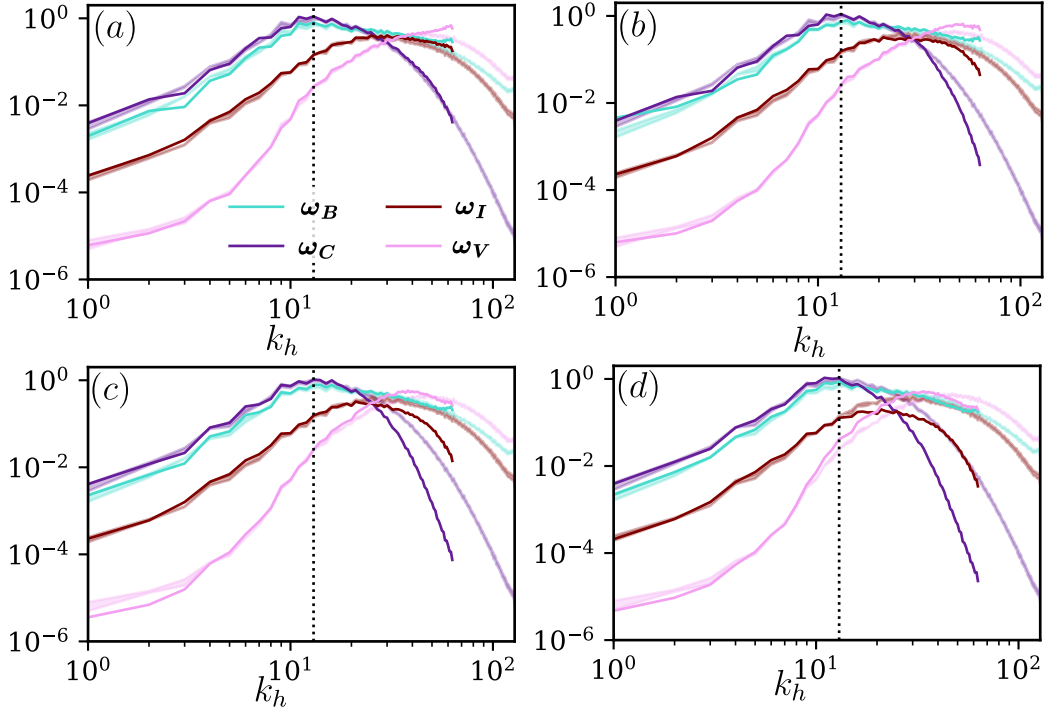


FIG. 9. Wave-number dependence of each vorticity contribution for each HD run. The shaded regions are the standard deviation surrounding the average of the DNS run at the same parameter regime. The dotted black line is k_{\perp} for each HD run. Case run at $Ra = 3.5 \times 10^8$, $\widetilde{Ra} = 10.12$, $Ek = 10^{-5}$, $Pr = 7$ and $\Gamma = 2$ with (a) $k_0 = 48$, (b) $k_0 = 32$, (c) $k_0 = 16$, (d) $k_0 = 8$.

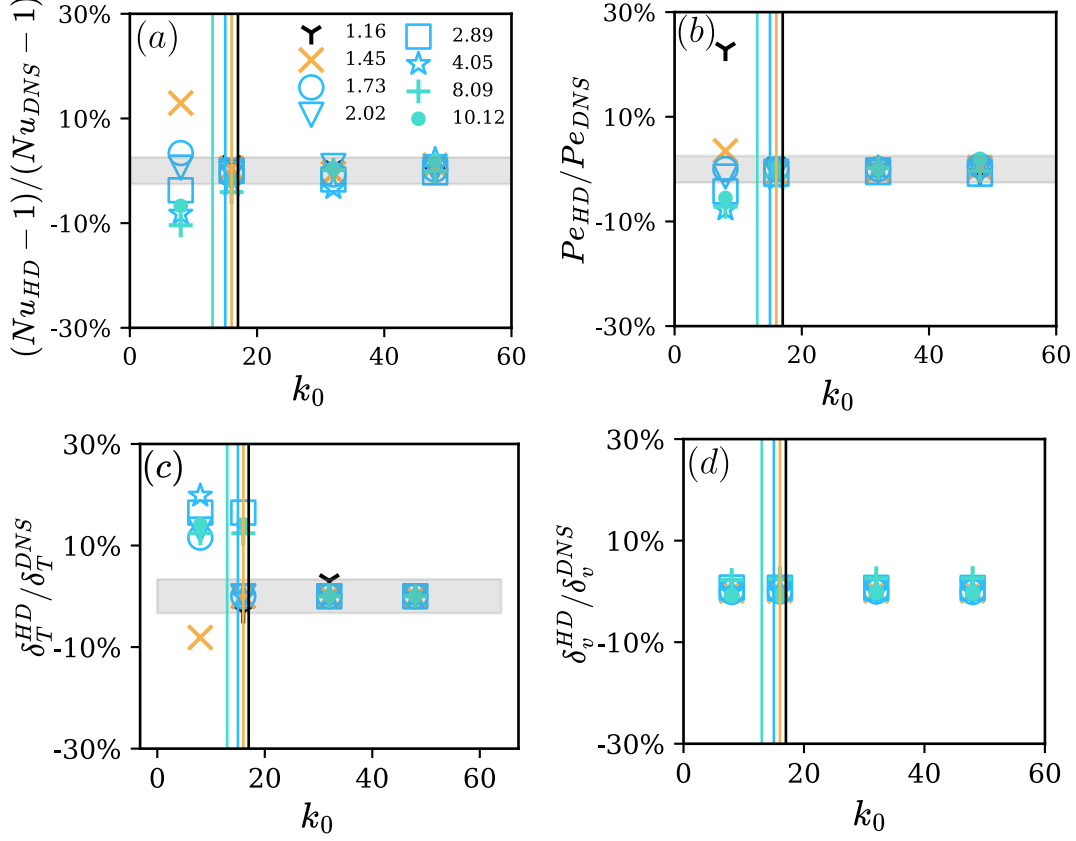


FIG. 10. (a) The ratio of the integral Nusselt number calculated in the HD runs to the Nusselt number calculated in the DNS runs is shown as a function of the cut-off wave-number k_0 . The shaded region represents the average standard deviation across all the DNS runs for Nu , Pe and δ_T . The perpendicular length scale is highlighted by colour for each run and shown as a vertical line. We present the runs as a function of $\widetilde{Ra} = Ra/Ra_c$ where $Ra_c = 3.45 \times 10^7$ (b) Péclet number Pe . (c) Thermal boundary layer thickness. (d) Viscous boundary layer thickness.

$\widetilde{Ra} = 1.16 - 10.12$, at fixed $Ek = 10^{-5}$, $Pr = 7$, and $\Gamma = 2$.

Figure 10 shows the percentage difference of Nu_I , Pe , δ_T , and δ_v between the DNS and the HD cases as a function of k_0 for different suites of \widetilde{Ra} simulations. δ_v is close to the DNS value for all k_0 as expected, while the HD value of Pe closely approximates the DNS value for all runs with $k_0 \geq k_\perp$. The heat transfer diagnostics are more sensitive to HD than δ_v and Pe . At $\widetilde{Ra} \leq 1.73$, HD with $k_0 = 8$ overestimates Nu and underestimates δ_T , while for $k_0 \geq k_\perp$ both quantities are within the standard deviation of their DNS values. At $\widetilde{Ra} \geq 4.05$ HD with $k_0 \leq 16$ underestimates Nu , while for $1.73 < \widetilde{Ra} \leq 4.05$ HD gives Nu within the standard deviation of the DNS value for all k_0 .

488 We now investigate the effect of HD as a function of Ek . We have run HD simulations
 489 at all DNS conditions shown in Figure 2. Figure 11 shows the scaling behaviour of Nu
 490 and Pe for both DNS and HD simulations, with the latter grouped according to values
 491 of k_0 in the ranges $k_0 < k_\perp$ and $2k_\perp < k_0 < 3k_\perp$. Across all Ek considered, the cases
 492 with $k_0 < k_\perp$ have increased Nu and Pe at low supercriticality and decreased Nu and Pe
 493 at high supercriticality, consistent with the results in Sections III A and III B. To further
 494 demonstrate that increased Nu and Pe are related to a decrease in the rotational constraint
 495 at low \widetilde{Ra} we conducted linear stability analysis for all Ek considered in this study (Table I).
 496 For HD with $k_0 < k_\perp$ there is a reduction in Ra_c compared to DNS at all Ek . This is also
 497 consistent with Figure 8, which shows that HD simulations with $k_0 = 8$ yield a larger
 498 dominant length scale compared to DNS at all Ek considered. For $2k_\perp < k_0 < 3k_\perp$, Figure
 499 11 shows good agreement between the DNS and HD at all Ek and Ra indicating that a
 500 value of k_0 between $2k_\perp$ and $3k_\perp$ is sufficient to yield large scale diagnostics within standard
 501 deviation of the DNS.

502 The black line in Figure 11a shows the approximate values of Ra at which HD runs
 503 with $k_0 = 8$ yield values of Nu and Pe within the standard deviation of the DNS. These
 504 lines, which delineate the transition between over/underestimation of Nu and Pe in the HD
 505 runs, occur at $\widetilde{Ra} \approx 1.85$. Comparison with Figure 2 shows that this transition does not
 506 correspond to a transition from VAC to IVAC balance in the vorticity equation. This is
 507 because the effect of HD is determined by the shape of the energy spectrum in our solutions.
 508 As \widetilde{Ra} increases, the peak in the energy spectrum of the solution broadens (see Figures 4 and
 509 7). At the transition in HD behaviour, a balance exists between the added energy due to a
 510 reduced Ra_c and the reduction of energy at small scales. In our simulations this transition
 511 occurs within the VAC regime.

512 We now analyse the scaling exponents predicted by HD simulations. We restrict attention
 513 to the VAC regime as this is well sampled by our dataset across 4 generations of Ek . We
 514 fit a function of the form $Nu = \alpha Ra^{\beta_{Nu}}$ and $Pe = \alpha Ra^{\beta_{Pe}}$ to data sets grouped by $k_0 < k_\perp$
 515 and $2k_\perp < k_0 < 3k_\perp$. Table II shows both β_{Nu} and β_{Pe} calculated for each data group. In
 516 the DNS β_{Nu} increases with decreasing Ek from 2.523 at $Ek = 10^{-4}$ to 3.660 at $Ek = 10^{-7}$,
 517 which is consistent with the results of Cheng *et al.* [36] and encompasses the $\beta_{Nu} = 3$ scaling
 518 of King *et al.* [43]. In the data sets where $2k_\perp < k_0 < 3k_\perp$, β remains within the standard
 519 deviation of the DNS runs. In the cases where $k_0 < k_\perp$, β_{Nu} is smaller than the DNS at all

Ek	Ra_c (DNS)	Ra_c (HD)	Difference
10^{-4}	1.53×10^6	1.40×10^6	9.28%
10^{-5}	3.45×10^7	3.13×10^7	11.0%
10^{-6}	7.59×10^8	6.87×10^8	10.5%
10^{-7}	1.69×10^{10}	1.49×10^{10}	13.4%

TABLE I. Ra_c for DNS and HD cases where $k_0 = 0.5k_\perp$ at each Ek considered in this study calculated using linear stability analysis.

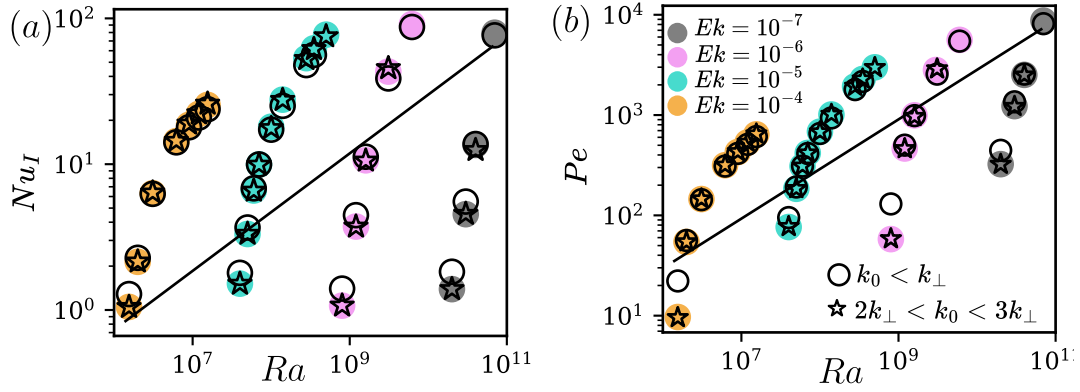


FIG. 11. Nusselt number (a) and Péclet number (b) plotted for all DNS runs and HD runs with $k_0 < k_\perp$ and $2k_\perp < k_0 < 3k_\perp$. The black line in (a) is fitted to the Ra which delineates the transition of increasing Nu and decreasing Nu for each Ek other than $Ek = 10^{-4}$.

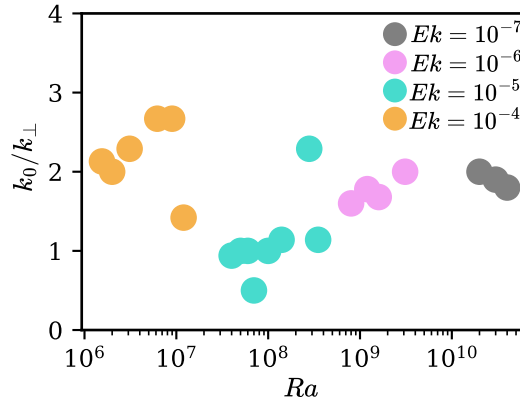


FIG. 12. The minimum k_0 for a Ra and Ek for which Nu and Pe in the HD remain within the standard deviation of the DNS.

Ek	10^{-4}	10^{-5}	10^{-6}	10^{-7}
β_{Nu} (DNS)	2.523 ± 0.054	3.161 ± 0.120	3.570 ± 0.145	3.660 ± 0.142
$\beta_{Nu} (2k_{\perp} < k_0 < 3k_{\perp})$	2.539	3.170	3.530	3.528
$\beta_{Nu} (k_0 < k_{\perp})$	2.412	2.955	3.137	3.067
β_{Pe} (DNS)	2.712 ± 0.023	3.192 ± 0.122	3.041 ± 0.152	2.682 ± 0.120
$\beta_{Pe} (2k_{\perp} < k_0 < 3k_{\perp})$	2.732	3.203	2.978	2.705
$\beta_{Pe} (k_0 < k_{\perp})$	2.443	2.831	2.598	2.365

TABLE II. Summary of the exponents calculated in the VAC regime for the DNS, HD runs conducted with $k_0 < k_{\perp}$ and HD runs conducted with $2k_{\perp} < k_0 < 3k_{\perp}$.

Ek . In the DNS β_{Pe} varies with Ek and covers a range from 2.712 to 3.192. Mirroring the results for β_{Nu} , data sets grouped by $2k_{\perp} < k_0 < 3k_{\perp}$ remain within the standard deviation of the DNS and cases with $k_0 < k_{\perp}$ were below the DNS for all Ek . For $k_0 < k_{\perp}$, both exponents are reduced at all Ek compared to the DNS because HD increases Nu and Pe at low supercriticality. Therefore, to obtain scaling behaviour consistent with DNS it is necessary to set $k_0 > k_{\perp}$.

Figure 12 shows the minimum value of k_0 in HD runs that produces a value of Nu within the standard deviation of the comparable DNS run, normalised by k_{\perp} . All runs other than $Ra = 7 \times 10^7$ require $k_0 > k_{\perp}$ to match Nu in the DNS. The run with $Ra = 7 \times 10^7$ exemplifies a case where the two effects of HD are in balance, and the energy increase coming from reducing Ra_c is in balance with the reduction of energy at small scales. This figure suggests that setting $k_0 = 3k_{\perp}$ is a conservative strategy in order for HD runs to produce large scale diagnostics consistent with DNS. More detailed knowledge of the changing effects of HD with Ek and Ra would allow k_0 to be reduced below this value.

D. The effect of changing the growth factor q

Figure 13 shows Nu and Pe for HD cases conducted at $Ra = 1.4 \times 10^8$, $Ek = 10^{-5}$, $Pr = 7$ and $\Gamma = 2$ with varying q and k_0 , normalised by Nu and Pe calculated in a DNS

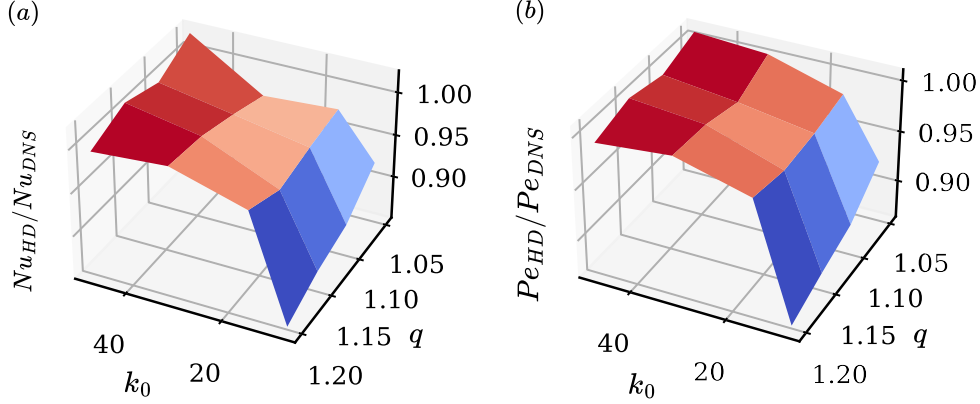


FIG. 13. Nusselt number (a) and Péclet number (b) calculated in the HD simulation respectively divided by the Nu and Pe calculated in the DNS runs conducted at $Ra = 1.4 \times 10^8$, $\widetilde{Ra} = 4.05$, $Ek = 10^{-5}$, $Pr = 7$ and $\Gamma = 2$.

run at the same parameters. In these runs, $\widetilde{Ra} = 4.05$, and therefore both Nu and Pe decrease when compared with the DNS. This effect is largest when $k_0 = 8$ and $q = 1.20$; these are the lowest k_0 tested and the highest q . The greatest similarity is the case where $k_0 = 48$ and $q = 1.05$. Over the range of values tested here, changing k_0 had a larger impact than changing q . All cases where $k_0 = 8$ resulted in reductions to Nu by at least 7.9% and Pe by at least 7.7%, which are greater differences than the standard deviation of the DNS. Whereas, when $q = 1.2$ and $k_0 = 48$, a reduction in Nu of 0.4% and Pe of 2% is observed. Figure 13 shows that the choice of k_0 is more important than the choice of q if the goal of the simulation is to understand flow speeds and heat transfer. The choice of k_0 has a greater impact in RRBC due to the concentration of energy around L_\perp .

E. Computational gain from hyperdiffusion

The aim of HD is to stabilise a simulation at a lower resolution, thus saving computational resources while not affecting the dynamics at the important scales. To investigate the potential computational gain, three simulations were carried out at $\widetilde{Ra} = 14.45$, $Pr = 7$, $\Gamma = 2$ and $Ek = 10^{-5}$, the first being a DNS run, the second and third utilising HD. To compare the computational demand of each simulation, we use the CPU hours needed to compute one convective time step, excluding the transient. The DNS case was run at a

554 resolution of (N_x, N_y, N_z) of (256, 256, 128) while the HD runs were conducted at resolutions
 555 of (192, 192, 128) (case 1) and (128, 128, 128) (case 2). In both cases, k_0 was set to $2k_\perp$
 556 and q was chosen so that both simulations have the same or greater peak-to-trough drop-off
 557 in kinetic energy as the DNS; $q = 1.073$ in case 1 and $q = 1.104$ in case 2. Additionally,
 558 we require that the HD simulation produces Nu , Pe , δ_θ and δ_v all within the standard
 559 deviation of the DNS. To ensure fair comparison, all three cases were run on the same HPC
 560 architecture (the UK facility ARCHER2) using the same compiled version of Dedalus and
 561 with identical distributions of processes across nodes.

562 The DNS run required 7983 CPU hours to compute one convective overturn, compared
 563 with 5855 hours for Case 1 (1.36 times faster than DNS) and 2263 CPU hours for Case
 564 2 (3.82 times faster than DNS). Although both runs had the same level of resolution and
 565 the boundary layers were within 1% of each other, both Nu_I and Pe were not within
 566 the standard deviation of the DNS in case 2. The computational savings are larger using
 567 this lower resolution, but the solution deviates meaningfully from the DNS. At $q = 1.104$,
 568 $k_0 = 2k_\perp$ is too small; achieving a workable HD run at this resolution would require a larger
 569 cut-off (e.g. approaching $3k_\perp$). Whether such an increase would stabilise the numerical
 570 scheme without degrading the large-scale dynamics may or may not hold.

571 IV. DISCUSSION AND CONCLUSIONS

572 In this paper we have analysed the influence of a scale-dependent horizontal form of
 573 hyperdiffusion (HD) on the large scale properties of rotating Rayleigh-Bénard convection.
 574 The HD function is applied to the horizontal directions and is controlled by two parameters:
 575 the wavenumber k_0 above which HD is applied, and the growth rate q such that the effect
 576 of HD scales with wavenumber k as q^{k-k_0} . In the range of parameters $Ek = 10^{-4} - 10^{-7}$,
 577 $Ra = 10^6 - 7 \times 10^{10}$ and $Pr = 7$ we have found two primary effects of HD on the large
 578 scale solution that are most prominent when $k_0 < k_\perp$. At low $\widetilde{Ra} = Ra/Ra_c$, the Nusselt
 579 number Nu and Péclet number Pe are increased compared to DNS due to a weakening of
 580 the rotational constraint, while at high \widetilde{Ra} , Nu and Pe are decreased compared to DNS
 581 owing to suppression of energy at scales $> k_\perp$. The thermal boundary layer thickness δ_T
 582 broadly follows the behaviour of Nu , while the mechanical boundary layer thickness δ_u is
 583 determined primarily by a vertical balance of terms and is therefore only marginally affected

by the HD. For $k \geq 3k_0$, all of the aforementioned diagnostics remain within the standard deviation of the DNS solution at all parameter combinations considered. This conclusion is broadly consistent with results obtained from recent dynamo simulations [19].

Quantifying the range of q values that yield acceptable performance of the HD scheme (i.e. large scale diagnostics within the standard deviation of the DNS) is challenging because it is linked to the chosen value of k_0 . For a high k_0 a larger q can be used without influencing the dynamics around the dominant energy scale k_\perp , while lower q values are needed for lower k_0 . Ultimately our results show that k_0 and q should be chosen so as to leave that the dynamics unaffected up to wavenumbers $\approx 2 - 3$ times k_\perp .

While our study consists of over 100 simulations, it is nevertheless limited to a single value of Pr and does not reach the very low values of Ek that have been achieved in recent simulations. Furthermore, we have considered only one form of the HD function. More work is needed to understand the effects of HD as these properties are varied. For now, our work and previous studies [13, 19] suggest that the form of the energy spectrum is crucial for the performance of the HD scheme. Our results show that a viable HD scheme should not affect some large scale component of the solution and we would expect this to be the case as control parameters and boundary conditions are varied.

It is clear that the implementation of any HD scheme will inevitably alter the behaviour of the solution at some scale. The choice to use a HD scheme should therefore be based in part on the scientific question that is to be addressed. When studying planetary cores it is generally the case that only the largest scales of the system can be recovered from observations, and so the goal of simulations is to develop scaling laws for large scale diagnostics (heat transfer, RMS velocity, etc). The computational gains of scale-dependent horizontal HD suggest that such schemes are a promising avenue for investigating the large scale dynamics of RRBC at more extreme physical conditions than are currently accessible via DNS.

However, care is required when implementing HD schemes, as our results suggest that large-scale quantities may not be faithfully recovered in HD simulations of RRBC unless the HD treatment is such that it does not strongly influence length scales containing significant energy.

ACKNOWLEDGMENTS

B.D. is supported by the Engineering and Physical Sciences Research Council (EPSRC) Centre for Doctoral Training in Fluid Dynamics (EP/S022732/1). S.M.T. was supported by funding from the European Research Council (ERC) under the EU’s Horizon 2020 research and innovation programme (grant agreement D5S-DLV-786780). C.D. acknowledges support from the Natural Environment Research Council (NERC) grant number (NE/V010867/1). J.E.M. acknowledges funding via a Natural Environment Research Council award, reference (NE/W005247/1). Calculations were performed on the UK national supercomputing facility ARCHER2 (<http://www.archer.ac.uk>) as well as ARC4, part of the High Performance Computer facilities at the University of Leeds.

DECLARATION OF INTERESTS

The authors report no conflict of interest.

Appendix A

Summary tables of the type of simulation, control parameters, resolution and selected output parameters. In all cases $Pr = 7$.

Type	Ek	Ra	$N_x = N_y$	N_z	Γ	k_0	Nu_I	Pe	δ_v	δ_T	E_b
DNS	10^{-4}	1.55×10^6	192	64	4	Na	1.05	9.69	0.0349	0.4991	0.001%
HD	10^{-4}	1.55×10^6	96	64	4	32	1.05	9.57	0.0349	0.4878	0.010%
HD	10^{-4}	1.55×10^6	96	64	4	8	1.29	22.18	0.0343	0.3842	0.001%
DNS	10^{-4}	2.00×10^6	192	64	4	Na	2.14	54.36	0.0331	0.1924	0.050%
HD	10^{-4}	2.00×10^6	96	64	4	32	2.15	54.54	0.0331	0.1963	0.040%
HD	10^{-4}	2.00×10^6	96	64	4	8	2.28	56.18	0.0331	0.1834	0.090%
DNS	10^{-4}	3.10×10^6	192	64	4	Na	6.32	145.4	0.0320	0.0776	0.110%
HD	10^{-4}	3.10×10^6	96	64	4	32	6.39	146.1	0.0320	0.0776	0.421%
HD	10^{-4}	3.10×10^6	96	64	4	8	6.26	143.4	0.0320	0.0776	0.143%
DNS	10^{-4}	6.20×10^6	192	64	4	Na	14.40	316.2	0.0312	0.0391	0.422%
HD	10^{-4}	6.20×10^6	96	64	4	32	14.44	316.7	0.0312	0.0429	0.124%
HD	10^{-4}	6.20×10^6	96	64	4	8	14.12	309.0	0.0312	0.0382	0.397%
DNS	10^{-4}	9.00×10^6	192	64	4	Na	18.63	428.8	0.0310	0.0252	0.562%
HD	10^{-4}	9.00×10^6	96	64	4	32	18.87	432.7	0.0310	0.0335	0.319%
HD	10^{-4}	9.00×10^6	96	64	4	8	17.91	415.4	0.0310	0.0330	0.971%
DNS	10^{-4}	1.20×10^7	192	64	4	Na	22.13	533.1	0.0307	0.0252	0.169%
HD	10^{-4}	1.20×10^7	96	64	4	32	22.31	536.3	0.0307	0.0252	0.532%
HD	10^{-4}	1.20×10^7	96	64	4	8	20.90	510.5	0.0307	0.02522	0.414%
DNS	10^{-4}	1.55×10^7	192	64	4	Na	25.49	641.9	0.0308	0.0252	0.451%
HD	10^{-4}	1.55×10^7	96	64	4	32	25.98	648.7	0.0307	0.0252	0.763%
HD	10^{-4}	1.55×10^7	96	64	4	8	23.81	610.3	0.0307	0.0252	0.330%
DNS	10^{-5}	3.20×10^7	256	128	2	Na	1.00	0.00	Na	Na	Na
HD	10^{-5}	3.20×10^7	128	128	2	8	1.09	25.54	Na	Na	Na
DNS*	10^{-5}	4.00×10^7	256	128	2	Na	1.51	76.50	0.0108	0.4511	0.009%
HD*	10^{-5}	4.00×10^7	128	128	2	48	1.51	75.73	0.0108	0.4025	0.010%
HD*	10^{-5}	4.00×10^7	128	128	2	32	1.52	76.38	0.0108	0.4146	0.012%
HD*	10^{-5}	4.00×10^7	128	128	2	16	1.52	77.20	0.0108	0.3905	0.011%
HD*	10^{-5}	4.00×10^7	128	128	2	8	1.80	94.03	0.0108	0.2222	0.020%
DNS	10^{-5}	5.00×10^7	256	128	2	Na	3.32	184.4	0.0107	0.0809	0.022%
HD	10^{-5}	5.00×10^7	128	128	2	48	3.33	185.4	0.0107	0.0809	0.030%
HD	10^{-5}	5.00×10^7	128	128	2	32	3.33	184.1	0.0107	0.0809	0.030%
HD	10^{-5}	5.00×10^7	128	128	2	16	3.34	184.7	0.0107	0.0809	0.030%

DNS	10^{-5}	1.40×10^8	256	128	2	Na	27.71	1013	0.0104	0.0165	0.361%
HD	10^{-5}	1.40×10^8	128	128	2	48	28.31	1021	0.0104	0.0165	0.382%
HD	10^{-5}	1.40×10^8	128	128	2	32	26.83	1016	0.0104	0.0165	0.327%
HD	10^{-5}	1.40×10^8	128	128	2	16	26.98	994.4	0.0104	0.0165	0.353%
HD	10^{-5}	1.40×10^8	128	128	2	8	25.52	935.9	0.0104	0.0197	0.330%
DNS	10^{-5}	2.80×10^8	256	128	2	Na	53.35	1925	0.0101	0.0096	0.714%
HD	10^{-5}	2.80×10^8	128	128	2	48	53.41	1926	0.0103	0.0096	0.506%
HD	10^{-5}	2.80×10^8	128	128	2	32	52.58	1936	0.0103	0.0096	0.524%
HD	10^{-5}	2.80×10^8	128	128	2	16	51.30	1906	0.0103	0.0108	0.390%
HD	10^{-5}	2.80×10^8	128	128	2	8	47.82	1800	0.0103	0.0108	0.211%
DNS+	10^{-5}	3.50×10^8	256	128	2	Na	62.31	2294	0.0104	0.0084	0.712%
HD+	10^{-5}	3.50×10^8	128	128	2	48	63.49	2334	0.0104	0.0084	0.509%
HD+	10^{-5}	3.50×10^8	128	128	2	32	61.55	2297	0.0104	0.0084	0.529%
HD+	10^{-5}	3.50×10^8	128	128	2	16	59.85	2282	0.0103	0.0096	0.393%
HD+	10^{-5}	3.50×10^8	128	128	2	8	56.15	2161	0.0103	0.0096	0.215%
DNS	10^{-5}	5.00×10^8	256	128	2	Na	77.31	2993	0.0104	0.0084	0.952%
DNS	10^{-6}	8.00×10^8	192	192	1	Na	1.07	57.96	0.0036	0.4959	0.001%
HD	10^{-6}	8.00×10^8	96	192	1	48	1.07	58.04	0.0036	0.4959	0.121%
HD	10^{-6}	8.00×10^8	96	192	1	32	1.07	58.51	0.0035	0.4714	0.121%
HD	10^{-6}	8.00×10^8	96	192	1	8	1.40	130.1	0.0036	0.3745	0.022%
DNS	10^{-6}	1.20×10^9	192	192	1	Na	3.75	464.1	0.0036	0.0571	0.435%
HD	10^{-6}	1.20×10^9	96	192	1	48	3.73	456.5	0.0036	0.0626	0.694%
HD	10^{-6}	1.20×10^9	96	192	1	32	3.76	464.0	0.0035	0.0626	0.694%
HD	10^{-6}	1.20×10^9	96	192	1	8	4.47	501.0	0.0036	0.00462	0.089%
DNS	10^{-6}	1.60×10^9	192	192	1	Na	10.63	9974.3	0.0035	0.0227	0.018%
HD	10^{-6}	1.60×10^9	96	192	1	48	10.58	972.1	0.0035	0.0227	0.650%
HD	10^{-6}	1.60×10^9	96	192	1	32	10.47	969.1	0.0035	0.0227	0.650%
HD	10^{-6}	1.60×10^9	96	192	1	8	11.25	977.9	0.0035	0.0227	0.610%
DNS	10^{-6}	3.10×10^9	192	192	1	Na	43.15	2812	0.0035	0.0088	0.491%
HD	10^{-6}	3.10×10^9	96	192	1	32	45.51	2888	0.0035	0.0088	0.654%
HD	10^{-6}	3.10×10^9	96	192	1	8	38.73	2559	0.0035	0.0102	0.510%
DNS	10^{-6}	6.20×10^9	192	192	1	Na	91.36	5618	0.0035	0.0043	0.781%
HD	10^{-6}	6.20×10^9	128	192	1	12	87.84	5459	0.0035	0.0060	0.787%

Type	Ek	Ra	$N_x = N_y$	N_z	Γ	k_0	q	Nu_I	Pe	δ_v	δ_T	E_b
HD	10^{-5}	1.40×10^8	128	128	2	48	1.10	27.57	1021	0.0104	0.0165	0.428%
HD	10^{-5}	1.40×10^8	128	128	2	32	1.10	27.35	998.4	0.0104	0.0165	0.982%
HD	10^{-5}	1.40×10^8	128	128	2	16	1.10	26.88	983.2	0.0104	0.0165	0.381%
HD	10^{-5}	1.40×10^8	128	128	2	8	1.10	24.66	903.8	0.0104	0.0198	0.893%
HD	10^{-5}	1.40×10^8	128	128	2	48	1.15	28.02	1019	0.0104	0.0150	0.424%
HD	10^{-5}	1.40×10^8	128	128	2	32	1.15	27.46	1007	0.0104	0.0150	0.980%
HD	10^{-5}	1.40×10^8	128	128	2	16	1.15	26.46	990.2	0.0104	0.0181	0.389%
HD	10^{-5}	1.40×10^8	128	128	2	8	1.15	23.85	884.1	0.0104	0.0216	0.893%
HD	10^{-5}	1.40×10^8	128	128	2	48	1.20	27.61	993.6	0.0105	0.0135	0.423%
HD	10^{-5}	1.40×10^8	128	128	2	32	1.20	27.74	1004	0.0106	0.0150	0.982%
HD	10^{-5}	1.40×10^8	128	128	2	16	1.20	27.08	992.9	0.0107	0.0181	0.386%
HD	10^{-5}	1.40×10^8	128	128	2	8	1.20	23.83	874.7	0.0106	0.0233	0.899%
HD	10^{-5}	5.00×10^8	192	128	2	24	1.073	75.33	2977	0.0104	0.0084	0.479%
HD	10^{-5}	5.00×10^8	128	128	2	24	1.104	72.94	2928	0.0104	0.0084	0.194%

TABLE IV. A summary of all other runs, all quantities have been time and spatially averaged.

-
- [1] G. A. Glatzmaier, engComputer simulations of jupiter’s deep internal dynamics help interpret what juno sees, Proceedings of the National Academy of Sciences - PNAS Inaugural Article, **115**, 6896 (2018).
- [2] G. A. Glatzmaier and P. H. Roberts, engA three-dimensional convective dynamo solution with rotating and finitely conducting inner core and mantle, Physics of the Earth and Planetary Interiors **91**, 63 (1995).
- [3] M. Heimpel, J. Aurnou, and J. Wicht, Simulation of equatorial and high-latitude jets on jupiter in a deep convection model, Nature **438**, 193 (2005).
- [4] H. Jones and J. Marshall, Convection with rotation in a neutral ocean: A study of open-ocean deep convection, Journal of Physical Oceanography **23**, 1009 (1993).

- [5] G. I. Taylor, Experiments with rotating fluids, Proceedings of the Royal Society of London. Series A, Containing Papers of a Mathematical and Physical Character **100**, 114 (1921).
- [6] J. Proudman, On the motion of solids in a liquid possessing vorticity, Proceedings of the Royal Society of London. Series A, Containing Papers of a Mathematical and Physical Character **92**, 408 (1916).
- [7] S. Braginsky and V. Meytlis, Local turbulence in the earth’s core, Geophysical Astrophysical Fluid Dynamics **55**, 71 (1990).
- [8] C. J. Davies, D. Gubbins, and P. K. Jimack, Scalability of pseudospectral methods for geodynamo simulations, Concurrency and Computation: Practice and Experience **23**, 38 (2011).
- [9] N. Schaeffer, D. Jault, H. C. Nataf, and A. Fournier, Turbulent geodynamo simulations: A leap towards earth’s core, Geophysical Journal International **211**, 1 (2017).
- [10] T. Schwaiger, T. Gastine, and J. Aubert, Force balance in numerical geodynamo simulations: a systematic study, Geophysical Journal International **219**, S101 (2019).
- [11] J. E. Mound and C. J. Davies, Longitudinal structure of earth’s magnetic field controlled by lower mantle heat flow, Nature Geoscience **16**, 380 (2023).
- [12] H.-C. Nataf and N. Schaeffer, Turbulence in the core, (2015).
- [13] J. Aubert, Approaching earth’s core conditions in high-resolution geodynamo simulations, Geophysical Journal International **219**, S137 (2019).
- [14] M. Lesieur, O. Métais, and P. Comte, *Large-eddy simulations of turbulence* (Cambridge university press, 2005).
- [15] Y. Shirian and A. Mani, Eddy diffusivity operator in homogeneous isotropic turbulence, Physical Review Fluids **7**, L052601 (2022).
- [16] M. Hammond and D. S. Abbot, Numerical dissipation strongly affects the equatorial jet speed in simulations of hot jupiter atmospheres, Monthly Notices of the Royal Astronomical Society **511**, 2313 (2022).
- [17] E. Grote, F. H. Busse, and A. Tilgner, engEffects of hyperdiffusivities on dynamo simulations, Geophysical Research Letters **27**, 2001 (2000).
- [18] K. Zhang and C. A. Jones, engThe effect of hyperviscosity on geodynamo models, Geophysical Research Letters **24**, 2869 (1997).
- [19] J. Aubert, T. Gastine, and A. Fournier, engSpherical convective dynamos in the rapidly rotating asymptotic regime, Journal of Fluid Mechanics **813**, 558 (2017).

- [20] B. A. Buffett, A comparison of subgrid-scale models for large-eddy simulations of convection in the earth’s core, *Geophysical Journal International* **153**, 753 (2003).
- [21] M. Germano, A proposal for a redefinition of the turbulent stresses in the filtered navier–stokes equations, *The Physics of Fluids* **29**, 2323 (1986).
- [22] H. Matsui and B. Buffett, Sub-grid scale model for dynamo simulations in a rotating plane layer model—dealing with unstructured grids, in *AGU Fall Meeting Abstracts*, Vol. 2005 (2005) pp. GP31A–0083.
- [23] H. Matsui and B. A. Buffett, Commutation error correction for large eddy simulations of convection driven dynamos, *Geophysical & Astrophysical Fluid Dynamics* **101**, 429 (2007).
- [24] H. Matsui and B. A. Buffett, A dynamic scale-similarity model for dynamo simulations in a rotating plane layer, *Geophysical and Astrophysical Fluid Dynamics* **101**, 451 (2007).
- [25] H. Matsui and B. A. Buffett, Large-eddy simulations of convection-driven dynamos using a dynamic scale-similarity model, *Geophysical & Astrophysical Fluid Dynamics* **106**, 250 (2012).
- [26] J. Boussinesq, *Théorie analytique de la chaleur: mise en harmonie avec la thermodynamique et avec la théorie mécanique de la lumière*, Vol. 2 (Gauthier-Villars, 1903).
- [27] G. Ahlers, S. Grossmann, and D. Lohse, Heat transfer and large scale dynamics in turbulent rayleigh–bénard convection, *Reviews of Modern Physics* **81**, 503 (2009).
- [28] K. Julien, E. Knobloch, A. M. Rubio, and G. M. Vasil, Heat transport in low-rossby-number rayleigh–bénard convection, *Physical review letters* **109**, 254503 (2012).
- [29] P. A. Gilman, Nonlinear dynamics of boussinesq convection in a deep rotating spherical shell-i, *Geophysical & Astrophysical Fluid Dynamics* **8**, 93 (1977).
- [30] T. Gastine, J. Wicht, and J. Aubert, Scaling regimes in spherical shell rotating convection, *Journal of Fluid Mechanics* **808**, 690 (2016).
- [31] R. S. Long, J. E. Mound, C. J. Davies, and S. M. Tobias, Thermal boundary layer structure in convection with and without rotation, *Physical Review Fluids* **5**, 113502 (2020).
- [32] R. E. Ecke and O. Shishkina, Turbulent rotating rayleigh–bénard convection, *Annual Review of Fluid Mechanics* **55**, 603 (2023).
- [33] S. Chandrasekhar, The instability of a layer of fluid heated below and subject to coriolis forces, *Proceedings of the Royal Society of London. Series A. Mathematical and Physical Sciences* **217**, 306 (1953).

- [34] R. P. J. Kunnen, B. J. GEURTS, and H. J. H. CLERCX, Experimental and numerical investigation of turbulent convection in a rotating cylinder, *Journal of Fluid Mechanics* **642**, 445–476 (2010).
- [35] A. Guzmán, M. Madonia, J. Cheng, R. Ostilla-Mónico, H. Clercx, and R. Kunnen, Force balance in rapidly rotating rayleigh–bénard convection, *Journal of Fluid Mechanics* **928** (2021).
- [36] J. S. Cheng, S. Stellmach, A. Ribeiro, A. Grannan, E. M. King, and J. M. Aurnou, Laboratory-numerical models of rapidly rotating convection in planetary cores, *Geophysical Journal International* **201**, 1 (2015).
- [37] J. S. Cheng, M. Madonia, A. J. A. Guzmán, and R. P. Kunnen, Laboratory exploration of heat transfer regimes in rapidly rotating turbulent convection, *Physical Review Fluids* **5**, 113501 (2020).
- [38] M. Sprague, K. Julien, E. Knobloch, and J. Werne, Numerical simulation of an asymptotically reduced system for rotationally constrained convection, *Journal of Fluid Mechanics* **551**, 141 (2006).
- [39] S. Maffei, M. J. Krouss, K. Julien, and M. A. Calkins, On the inverse cascade and flow speed scaling behaviour in rapidly rotating rayleigh–bénard convection, *Journal of Fluid Mechanics* **913**, A18 (2021).
- [40] J. M. Aurnou, S. Horn, and K. Julien, Connections between nonrotating, slowly rotating, and rapidly rotating turbulent convection transport scalings, *Physical Review Research* **2**, 043115 (2020).
- [41] J. Song, O. Shishkina, and X. Zhu, Scaling regimes in rapidly rotating thermal convection at extreme rayleigh numbers (2023), arXiv:2304.14854 [physics.flu-dyn].
- [42] H. P. Greenspan, *The theory of rotating fluids*, Tech. Rep. (Massachusetts Inst of Tech Cambridge Dept of Mathematics, 1968).
- [43] E. M. King, S. Stellmach, and J. M. Aurnou, Heat transfer by rapidly rotating rayleigh–bénard convection, *Journal of Fluid Mechanics* **691**, 568 (2012).
- [44] E. M. King, K. M. Soderlund, U. R. Christensen, J. Wicht, and J. M. Aurnou, Convective heat transfer in planetary dynamo models, *Geochemistry, Geophysics, Geosystems* **11** (2010).
- [45] K. M. Soderlund, A. Sheyko, E. M. King, and J. M. Aurnou, The competition between lorentz and coriolis forces in planetary dynamos, *Progress in Earth and Planetary Science* **2**, 1 (2015).

- [46] W. Kuang, B. Chao, and J. Chen, Decadal polar motion of the earth excited by the convective outer core from geodynamo simulations, *Journal of Geophysical Research: Solid Earth* **122**, 8459 (2017).
- [47] C. Dong, H. Zhang, L. Jiao, H. Cheng, D. A. Yuen, and Y. Shi, The non-negligible effect of viscosity diffusion on the geodynamo process, *Journal of Geophysical Research: Solid Earth* **126**, e2020JB021281 (2021).
- [48] J. Aubert, State and evolution of the geodynamo from numerical models reaching the physical conditions of Earth’s core, *Geophysical Journal International* **235**, 468 (2023), <https://academic.oup.com/gji/article-pdf/235/1/468/50615243/ggad229.pdf>.
- [49] O. Barrois, T. Gastine, and C. C. Finlay, Quasi-geostrophic convection-driven dynamos in a thick spherical shell, *Geophysical Journal International* **236**, 1373 (2024).
- [50] A. Oberbeck, Über die wärmeleitung der flüssigkeiten bei berücksichtigung der strömungen infolge von temperaturdifferenzen, *Annalen der Physik* **243**, 271 (1879).
- [51] K. J. Burns, G. M. Vasil, J. S. Oishi, D. Lecoanet, and B. P. Brown, Dedalus: A flexible framework for numerical simulations with spectral methods, *Physical Review Research* **2**, 10.1103/physrevresearch.2.023068 (2020).
- [52] A. Tilgner, A. Belmonte, and A. Libchaber, Temperature and velocity profiles of turbulent convection in water, *Physical Review E* **47**, R2253 (1993).
- [53] A. Belmonte, A. Tilgner, and A. Libchaber, Temperature and velocity boundary layers in turbulent convection, *Physical Review E* **50**, 269 (1994).
- [54] B. I. Shraiman and E. D. Siggia, Heat transport in high-rayleigh-number convection, *Physical Review A* **42**, 3650 (1990).
- [55] D. W. Hughes and F. Cattaneo, Force balance in convectively driven dynamos with no inertia, *Journal of Fluid Mechanics* **879**, 793 (2019).
- [56] E. Dormy, Strong-field spherical dynamos, *Journal of Fluid Mechanics* **789**, 500 (2016).
- [57] R. J. Teed and E. Dormy, Solenoidal force balances in numerical dynamos, *Journal of Fluid Mechanics* **964**, A26 (2023).
- [58] E. King, S. Stellmach, and B. Buffett, Scaling behaviour in rayleigh–bénard convection with and without rotation, *Journal of Fluid Mechanics* **717**, 449 (2013).
- [59] D. J. Stevenson, Turbulent thermal convection in the presence of rotation and a magnetic field: a heuristic theory, *Geophysical & Astrophysical Fluid Dynamics* **12**, 139 (1979).

- 762 [60] S. Grossmann and D. Lohse, Scaling in thermal convection: a unifying theory, *Journal of Fluid*
763 *Mechanics* **407**, 27 (2000).
- 764 [61] M. Madonia, A. J. A. Guzmán, H. J. Clercx, and R. P. Kunnen, Reynolds number scaling and
765 energy spectra in geostrophic convection, *Journal of Fluid Mechanics* **962**, A36 (2023).
- 766 [62] W. V. R. Malkus, engThe heat transport and spectrum of thermal turbulence, *Proceedings of*
767 *the Royal Society of London. Series A, Mathematical and Physical Sciences* **225**, 196 (1954).